Newly formed craters on Mars located using seismic and acoustic wave data from InSight

Raphael Garcia, Ingrid Daubar, Éric Beucler, Liliya Posiolova, Gareth Collins, Philippe Lognonné, Lucie Rolland, Zongbo Xu, Natalia Wójcicka, Aymeric Spiga, et al.

Title:
Newly formed craters on Mars located using seismic and acoustic wave data from InSight

Authors:
Raphael F. Garcia(1), Ingrid J. Daubar(2), Éric Beucler(3,4), Liliya Posiolova(5), Gareth S. Collins(6), Philippe Lognonné(7), Lucie Rolland(8), Zongbo Xu(7), Natalia Wójcicka(6), Aymeric Spiga(9,10) , Benjamin Fernando(11), Gunnar Speth(5), Léo Martire(12), Andrea Rajšić(13), Katarina Miljković(13), Eleanor K. Sansom(13), Constantinos Charalambous(14), Savas Ceylan(15), Sabrina Menina(7), Ludovic Margerin(16), Rémi Lapeyre(17), Tanja Neidhart(13), Nicholas A. Teanby(18), Nick Schmerr(19), Mickaël Bonnin(3,4), Marouchka Froment (7,20), John F. Clinton(21), Ozgur Karatekin(22), Simon C. Stähler(15), Nikolaj L. Dahmen(15) , Cecilia Durán(15) , Anna Horleston(18), Taichi Kawamura(7), Matthieu Plasman(7), Géraldine Zenhäusern(15), Domenico Giardini(15), Mark Panning(12), Mike Malin(5), William Bruce Banerdt(12)

(1) Institut Supérieur de l'Aéronautique et de l'Espace (ISAE-SUPAERO), Université de Toulouse, 10 Ave E. Belin 31400 Toulouse, France
(2) Brown University, Providence, RI, 02878, USA
(3) Nantes Université, Université Angers, Le Mans Université, CNRS, UMR 6112, Laboratoire de Planétologie et Géosciences, F-44000 Nantes, France
(4) Nantes Université, UGE, Univ Angers, CNAM, CNRS, UAR 3281, Observatoire des sciences de l'univers Nantes Atlantique, F-44000 Nantes, France
(5) Malin Space Science Systems, San Diego, USA
(6) Department of Earth Science and Engineering, Imperial College, London, SW7 2AZ, UK
(7) Université Paris Cité, Institut de physique du globe de Paris, CNRS, F-75005 Paris, France
(8) Université Côte d'Azur, Observatoire de la Côte d'Azur, CNRS, IRD, Géoazur, 250 rue Albert Einstein, Sophia Antipolis 06560 Valbonne, France
(9) Laboratoire de Météorologie Dynamique / Institut Pierre-Simon Laplace (LMD/IPSL), Sorbonne Université, Centre National de la Recherche Scientifique (CNRS), École Polytechnique, École Normale Supérieure (ENS)
(10) Institut Universitaire de France (IUF)
(11) Department of Physics, University of Oxford, UK
(12) Jet Propulsion Laboratory, California Institute of Technology, Pasadena, CA 91109, USA
(13) Curtin University, School of Earth and Planetary Sciences, Space Science and Technology Centre, Perth, Western Australia
(14) Department of Electrical and Electronic Engineering, Imperial College London, London, UK
(15) Institute of Geophysics, ETH Zurich, Zurich, Switzerland
(16) Institut de Recherche en Astrophysique et Planétologie, Université Toulouse III Paul Sabatier, CNRS, CNES, 14 Av. E. Belin, 31400, Toulouse, France.
(17) Centre National d'Etudes Spatiales, 18 Av. E. Belin, Toulouse, France
(18) School of Earth Sciences, University of Bristol, Bristol, UK
(19) Department of Geology, University of Maryland, College Park, MD, USA.
(20) Earth and Environmental Sciences Division, Los Alamos National Laboratory, Los Alamos, NM 87545,
(21) Swiss Seismological Service, ETH Zurich, Zurich, Switzerland
(22) Royal Observatory of Belgium, Brussels, Belgium

Abstract/summary (<200 words):
Meteoroid impacts shape planetary surfaces by forming new craters and alter atmospheric composition. During atmospheric entry and impact on the ground, meteoroids excite transient acoustic and seismic waves. However, new crater formation and the associated impact-induced mechanical waves have yet to be observed jointly beyond Earth. Here we report observations of seismic and acoustic waves from the NASA InSight lander's seismometer that we link to four meteoroid impact events on Mars observed in spacecraft imagery. We analyzed arrival times and polarization of seismic and acoustic waves to estimate impact locations, which were subsequently confirmed by orbital imaging of the associated craters. Crater dimensions and estimates of meteoroid trajectories are consistent with waveform modeling of the recorded seismograms. With identified seismic sources, the seismic waves can be used to constrain the structure of the Martian interior, corroborating previous crustal structure models, and constrain scaling relationships between the distance and amplitude of impact-generated seismic waves on Mars, supporting a link between the seismic moment of impacts and the vertical impactor momentum. Our findings demonstrate the capability of planetary seismology to identify impact-generated seismic sources and constrain both impact processes and planetary interiors.

Main text (<2000 words) – limit to 250 words per section:

Meteoroid impacts shape planetary surfaces and seed their atmospheres with exogenous volatiles. The mechanical waves generated by impacts are used to infer the structure of the atmosphere and the planet's interior, and to investigate current planetary impact processes. However, a clear link between recorded seismic and acoustic waves and a given impact crater has never before been accomplished on another planet. On Earth, meteoroid airburst events have been reported numerous times [1,2,3], but a hypervelocity impact with the ground was recorded only once [4]. Although numerous impacts were detected on the Moon by the Apollo seismic network [5,6], no natural impact was associated with visual detection of a new crater. SEIS (Seismic Experiment for Internal Structure) [7] and pressure [8,9] sensors on the InSight lander [10] provide a unique opportunity to relate martian meteoroid entry in the atmosphere and ground impact processes to the mechanical waves they generate [11]. We use InSight seismic data to estimate locations of new impact craters on Mars. Orbital imaging provides ground truth for these seismic sources. These seismic-imagery associations constrain distance-amplitude scaling relationships relating the impact processes to the seismic and acoustic waves, and further constrain crustal and atmospheric structure.

Impacts location and orbital imaging

Hypervelocity meteoroids generate shock waves, which decay into acoustic and seismic waves, upon atmospheric entry and fragmentation, and through impact on the ground [12,13,14]. During the Martian night, impact-generated acoustic waves can propagate over long distances in the downwind direction due to a thin near-surface atmospheric waveguide less than one kilometer thick [15] (**Fig. 1b**). Such guided acoustic waves generated by surface explosions have been observed on Earth as dispersed pressure wave trains [16,17]. In 2021, three seismic events with dominant energy above 5 Hz were located within 300 km of the InSight lander [18]. Their seismic records include comparable dispersed signals in the 0.4-4 Hz frequency range (**Fig. 1c, Extended data Fig. 1-2-3**). Each impact seismic event is named by sol number according to the InSight convention [19]. Due to lander power constraints, pressure and wind data for these events are not available. However, ground deformation recorded by the SEIS seismometer allows us to detect the acoustic waves through compliance effects [20,21]; an effect also observed on Earth for seismometers deployed on low velocity materials [22]. The peak amplitudes of vertical ground motions associated with the detected acoustic waves range from 27 nm/s to 0.9 nm/s in the 0.5-1.5Hz bandwidth, corresponding to acoustic waves of 45 to ~1.5 mPa, close to or below the pressure sensor noise level of ~10 mPa rms [9]. These motions exhibit a vertical retrograde elliptical polarization in a plane aligned with the direction of the incoming acoustic wave [15,20]. Due to low winds in the surface waveguide, deviations smaller than 5° are expected between this direction and the back azimuth of the source (**Extended Data Fig. 4**). The impact event distance and origin time are estimated by measuring the arrival times of acoustic and seismic P and S waves, under the assumptions that the P to S velocity ratio is equal to $\sqrt{3}$ (i.e. a Poisson solid), and that sound velocity and winds are those predicted by the Mars Climate Database (MCD) [23]. An impact location is calculated for each of these events with an uncertainty of +/-10% on distance and varying from +/-5° to +/-60° on back azimuth, depending on the signal-to-noise ratio (**Tab. 1**).

The Context Camera (CTX) on the Mars Reconnaissance Orbiter [24] selectively targets the surface of Mars for various scientific objectives. Repeated imaging of the region surrounding InSight allows identification of new impact craters. Using impact locations

estimated by the InSight team from seismic events S0793a, S0981c and S0986c, the CTX team confirmed the presence of three impact sites (**Fig. 2, Tab. 1**). They were identified by observing extended dark blast zones surrounding new impact craters that were not present in previous CTX images with 6 m/pixel resolution [25]. Each associated impact site falls within the corresponding seismic location error-ellipse and has before and after images by CTX that bracket the seismic origin time. Assuming cratering occurs as a Poisson process and using recent estimates of cratering rates [11], the probabilities of impacts occurring independent of the seismic events, but within the error-ellipse areas and the time intervals between images , are 0.18%, 2.24% and 0.02% for events S0793a, S0981c and S0986c respectively. The InSight team also provided a potential impact location for event S1034a, but despite an extensive search by the CTX team, no corresponding impact site could be found. The seismic and infrasound waves associated with this event could be due to a meteoroid airburst that did not create a visible change on the surface [14]. Independently, an impact cluster was discovered by CTX during routine imaging and later associated with the seismic event S0533a, which has a consistent location and time (**Tab. 1, Extended data Fig. 3**). Infrasound signals are also observed with this event. However, the low signal to noise ratio of SEIS records does not allow for an in-depth analysis. Higher resolution images of each of these sites were acquired by the High Resolution Imaging Science Experiment (HiRISE) [26] at 25 cm/pixel to detail the impact characteristics such as crater diameters (**Supplementary Information Tab. 1, Supplementary Information Fig. 1**).

Hearing meteoroid entry, fragmentation and impact

For three out of the four impact events, a single dispersive acoustic arrival is observed (**Extended data Fig. 1-2-3**). Two of these events are associated with the orbital detection of a single impact crater. In each case, the acoustic arrival is attributed to acoustic waves generated by the meteoroid's impact with the ground. The impact at the estimated location of event S0986c generated a cluster of multiple craters (**Fig. 2**), implying one or more atmospheric disruption events of the meteoroid along the entry path. Two polarized arrivals are observed in the SEIS record (A1, A2 in **Fig. 1**), which emanate from two different points along the impactor trajectory. The first event (A1) is either the entry shock wave or a fragmentation event. The second event (A2) is interpreted as a fragmentation event which produced the observed crater cluster. Conversion of the acoustic waves from the A2 atmospheric source to seismic waves at the surface generated the strong seismic signals observed around 2.4 Hz frequency and starting 55 s after the first seismic arrivals (X1). By combining the impact location, the infrasound polarization directions, and the arrival times, the altitude of the A2 acoustic source is estimated to be 13-16 km. From this geometry we estimate an entry angle of 30°±8° and an altitude of 26±8 km for the A1 acoustic source. These ranges are confirmed by full waveform simulations of seismic data (**Extended Data Fig. 5**), and are consistent with martian meteoroid entry predictions [27] (**Tab. 3**). The multiple impacts of meteoroid fragments with the ground excited acoustic waves that propagated in the low atmosphere waveguide, and are responsible for the main dispersed signal (A3) that was used to estimate the impact location. Additionally, a rumble of acoustic echos was created by acoustic wave scattering in the atmosphere and on the surface topography. Those echos were identified from their high coherence and 90° phase shift between the vertical and horizontal component of SEIS in the 0.5-2 Hz frequency range (**Fig. 1d-e**).

In these unique cases for which the distance to the seismic source is known, the origin time, P wave velocity and sound wave velocity can be re-calculated from P, S and acoustic arrival times (**Tab. 1**). As a consequence, the P wave propagation time is known as a function of distance. Within error bars, the observed times match those predicted by P waves traveling through the crustal layers in the reference internal structure model KKS21_GP [28,29] (**Fig. 3a**), thus validating the crust models produced from InSight seismic data.
The observed records of acoustic waves depend on the impact source, low atmosphere waveguide structure, and acoustic attenuation and compliance. The absence of acoustic waves above 4 Hz in all our observations confirms that acoustic attenuation controls this cut-off frequency [20]. The dispersion of the acoustic signal is correctly reproduced by atmospheric models (**Extended Data Fig. 6**). Additionally, differences in effective sound speed allow us to recover wind speeds in the lower atmosphere along the acoustic propagation path.

Impact rate and acoustic/seismic source estimates
The observed rate of small impacts based on orbital images [30,31] predicts 0.1 impacts per Earth year >3.9 m diameter in any 100 km radius circle. In previous work, we predicted InSight would detect ~0.2-20 impacts per Earth year [32, 33]. Thus the four impact events that we observe are reasonable to expect over the three years of the mission. However, it is surprising that they all occurred within a fairly short time period. Detection of the acoustic signals that enabled their identification and location do require a certain impact geometry and specific atmospheric conditions to propagate to the lander [15,18], as well as low noise levels, so that could partially explain why they have been identified only at certain times.
The observed crater diameter(s) for each event can be used to determine probability distributions of impactor parameters using statistical models of atmospheric entry of small meteoroids on Mars [27] (**Tab. 3**). A key impactor parameter for scaling the amplitude and seismic moment of impact-generated seismic waves is impactor vertical momentum at the ground [34, 35, 11]. Estimates of impactor momentum for the detected impact events are in the range 0.5-2x10^5 Ns. Predicted ground velocity time series at InSight's location are simulated using the full waveform modeling tool SPECFEM2D-DG-LNS [36]. From the amplitude scaling of acoustic and seismic P waves, we estimate the total energy, or yield, of each atmospheric source and the seismic moment of each ground impact. Atmospheric explosions at 26 km, 15 km and 0 km altitude used to simulate acoustic signals of event S0986c present yield values in the range 0.3-7.7 GJ (**Tab. 2**) which are compatible with estimates of total energy deposition in the atmosphere of 4.7-14 GJ (**Extended Data Fig. 7**). The same approach is used to estimate the yield and seismic moment for the other impact events (**Tab. 2** and **Tab. 3**). The yield estimates for the impacts are close to the predicted scaling relationship between crater diameter and yield [36]. The seismic moment estimates confirm the relationship between the seismic moment of impacts and the vertical impactor momentum [34, 35, 11] (**Fig. 3c**).

Comparative planetary seismology
The seismic source time function of impacts is also determined from the spectra of seismic first arrivals **(Extended Data Fig. 8)**. The cut-off frequencies of these estimates (**Tab. 3**) as a function of crater diameter are consistent with previous estimates [11,37] and are larger than those observed on the Moon [35] for comparable vertical impact momentum, likely as a consequence of the larger regolith seismic velocities on Mars than on the Moon [38]. With its larger signal-to-noise ratio, the impactor vertical momentum of S0986c can be independently estimated following methodology developed for the Lunar artificial impacts

[34], which provides additional constraints on attenuation and diffusion length scale. The comparison of S0986c on Mars and the LEM12 impact on the Moon (**Extended Data Fig. 9**), which was detected at a distance of 73 km by the Apollo 12 LP seismometer, confirms both the proportionality of wave amplitude with impactor vertical momentum and the larger attenuation of the martian subsurface and likely larger diffusion scale of Mars as compared to the Moon, as suggested by previous seismological analysis [38]. When scaled by impactor momentum, the peak P-wave amplitudes of impact-generated seismic signals detected on Mars (in the range 3 - 8 Hz), Earth and the Moon (in the range 1-16 Hz [39,40]) show a consistent trend with distance from the source, where amplitude decays with distance to the power -1.56 (**Extended Data Fig. 10).** Because P waves diffracted on crustal interfaces have a low amplitude compared to the rest of the seismic waves, this scaling is a lower bound of seismic amplitudes. However, this consistency between Mars and the Moon suggests that this can be applied to different planets. Such scaling laws justify the capabilities of future seismometers and infrasound sensors to measure impact rates and use meteoroid impacts as seismic sources to reach their science objectives.

Corresponding author:
Correspondence and requests for materials should be addressed to Raphael F. Garcia (raphael.garcia@isae.fr)

Acknowledgements:
This study is InSight contribution number 241 and LA-UR-22-25144.
The French authors acknowledge the French Space Agency CNES and ANR (ANR-14-CE36-0012-02 and ANR-19-CE31-0008-08) for funding the InSight Science analysis. IJD was supported by NASA grant 80NSSC20K0971. PL, ZX, SM, MF, TK, MP acknowledge IdEx Université de Paris ANR-18-IDEX-0001. NW and GC are funded by the UK Space Agency (Grants ST/S001514/1 and ST/T002026/1). NAT and AH are funded by the UK Space Agency (grants ST/R002096/1 and ST/W002523/1). MF is funded by the Center for Space and Earth Science of Los Alamos National Laboratory.
The authors thank CALMIP (Toulouse, France, project #p1404) computing center for HPC resources. We acknowledge NASA, CNES, their partner agencies and Institutions (UKSA, SSO, DLR, JPL, IPGP-CNRS, ETHZ, IC, MPS-MPG) and the flight operations team at JPL, SISMOC, MSDS, IRIS-DMC and PDS for providing SEED SEIS data. We are grateful to the CTX and HiRISE operations teams who planned and acquired the orbital images of the new impacts. We thank three anonymous reviewers for their constructive reviews that significantly improved this paper.

Author Contributions
R.F.G provided seismic locations of impacts and full waveform simulations. I.D., L.P. and G.S. planned orbital imaging acquisition and performed analysis of these images. E.B. and M.B. provided the seismological analysis and impact interpretation of seismic data. G.S.C. and N.W. provided impact trajectory analysis, impactor momentum estimates and amplitude scaling of seismic response for different planets. P.L. provided the analysis of the seismic source time function and the comparison of waveforms between Mars and Moon data. L.R., Z.X., L.M., M.F. and O.K. provided analysis of acoustic signal propagation in the atmosphere of Mars. A.R., K.M., E.K.S. and T.N. provided analysis of crater cluster dispersion. C.C., S.C., J.F.C., S.C.S., N.L.D, C.D., A.H., T.K., M.P. and G.Z. provided seismic event detections and seismic arrival times in the framework of Mars Quake Service front line team. S.M. and L.M. provided seismic arrival times and seismic

waveforms analysis of impact events. R.L. provided operational support on SEIS data and a sonification of SEIS records. N.A.T. provided scaling relations between seismic and impact parameters. N.S. provided analysis of impact cluster effect on seismic source estimates. D.G. and M.P. provided constructive analysis of the paper and text proofreading. M.M. is principal investigator of the CTX camera. P.L. is principal investigator of the SEIS instrument. W.B.B. is principal investigator of the InSight mission.

Competing interests
The authors declare no competing interests.

Tables:

Event name	S0986c	S0793a	S0981c	S0533a
UTC date (at event start time)	2021-09-05	2021-02-18	2021-08-31	2020-05-27
UTC time (at event start time)	05:23:58.00	19:36:23.00	04:04:01.00	13:48:26.00
Local True Solar Time (at event start time)	21:20:33	18:05:07	23:14:43	17:08:46
Median P wave arrival Time (UTC)	5:24:00	19:36:24.0	4:04:04	13:48:13
Median S-P time (s)	11.8	13.3	37.4	59.0
Median acoustic-P time (s)	331.9	336.0	991.4	1013.0
Sound speed from MCD (m/s)	247.0	236.0	258.0	262.0
Est. back azimuth (deg)	113 ±5	280.0 ±60	180.0 ±10	0.0 ±50
Est. distance (km)	86 ±9	84 ±8	267 ±25	286.5 ±50
Est. P velocity velocity (km/s)	5.3 ±0.6	4.6 ±0.5	5.2 ±0.5	3.6 ±1.2
Est. P wave propagation time (s)	16.1 ±5	18.2 ±7	51.0 ±8	80.6 ±15
Est. origin time	5:23:44	19:36:06	4:03:13	13:46:52
Orbital imaging latitude N (deg)	3.974	4.606	0.397	9.382
Orbital imaging longitude E (deg)	136.963	134.087	135.688	135.377
Date of Before Image	2021-04-02	2020-12-03	2018-03-25	2019-04-17
Date of After Image	2021-11-30	2021-06-10	2021-12-28	2021-07-31
Distance from orbital imaging (km)	85.1	91.1	243.6	289.0
Observed crater diameter(s) (m)	6.1 (effective diameter of cluster*)	3.9	7.2	11.9 (effective diameter of cluster*)
Back azimuth from orbital imaging (deg)	111.6	274.2	179.2	357.14
Est. P wave velocity (km/s) from imaging location	5.3 ±0.6	5.0 ±0.5	4.9 ±0.5	3.6 ±1.2
Est. effective sound speed (m/s) from imaging location	244.5	257.2	242.0	265.2
Est. origin Time from imaging location (UTC)	5:23:44	19:36:06	4:03:13	13:36:52

Est. P wave propagation time (s)	16.1 ±4.6	18.2 ±7.5	51.1 ±7.8	80.6 ±15

Tab. 1| Seismic and imaging parameters of impact events.
Absolute times are provided in Coordinated Universal Time (UTC). Impact locations are provided in the planetocentric geographical reference frame. Sound speed is extracted from Mars Climate Database (MCD). Back azimuth is relative to North and counted positive in the clockwise rotation sense. “Est.” means “Estimated”. First estimated values are from SEIS records only. Then, P wave velocity, effective sound speed, and Origin time are estimated using the known impact location.
*For individual crater diameters in clusters, see **Supplementary Information Tab. 1**.

Event	S0986c A.B. 1	S0986c A.B. 2	S0986c Impact	S0793a Impact	S0981c Impact
Crater Diameter (m)			5.5	3.9	7.2
Yield (J) estimated from SPECFEM2D Full waveform simulation scaling in 0.5-1.5 Hz range	2.5E+8	7.7E+9	3.4E+9	5.5E+8	1.6E+9
Yield (J) estimated from crater diameter [55]			1.4E+9	4.8E+8	4.1E+9

Tab. 2| Estimates of the energy (yield) of the acoustic sources
From top to bottom, event name, crater diameter, and yield estimated from SPECFEM2D-DG simulations and yield from crater diameter by using a scaling based on nuclear explosions [55]. Yield values are provided in Joules (J). Error bars on yield estimates from simulations are at least ±50%.

Method\Event	S0986c Impact	S0793a Impact	S0981c Impact
Observed diameter of the main crater (m)	5.7	3.9	7.2
Seismic moment from SPECFEM2D Full waveform simulation scaling (5.0-8 Hz) of an explosion (Nm)	1.3E+9 - 8.0E+9	5.4E+8 - 3.2E+9	1.5E+10 - 2.4E+12
Mars Quake Service magnitude estimate (Mw)	1.2	1.4	1.6
Frequency cut-off of seismic source (Hz)	8.0	9.4	
Median impactor	242000	55000	252000

momentum (Ns)			
Interquartile range (Ns)	208000--300000	43100--75600	210000--341000
Median vertical impactor momentum (Ns)	89500	27000	202000
Interquartile range (Ns)	80000 - 97000	22000 - 33000	183000 - 228000
Median impact energy (J)	7.20E+08	1.60E+08	1.00E+09
Interquartile range (J)	5.6E8 - 8.9E8	1.2E8 - 2E8	0.7E9 - 1.2E9
Median impactor mass (ground) (kg)	42.1	10.6	33.7
Interquartile range (kg)	36.6 - 51.1	6.3 - 15.7	26.2 - 52.6
Median impactor velocity (ground) (m/s)	5770	5450	6880
Interquartile range (m/s)	4990 - 6850	4500 - 7200	5940 - 9050
Mean Impact angle (ground) (deg)	21	31	55
Impact angle standard deviation (deg)	2.69	12.3	16.8
Median pre-entry mass (kg)	71	22.2	49.2
Interquartile range (kg)	57.8 - 81.3	17.4 - 30.6	38.2 - 70.7
Median energy deposited in air (J)	1.96E+09	8.68E+08	1.09E+09
Interquartile range (J)	1.0E9 - 2.9E9	4.5E8 - 1.48E9	0.64E9 - 1.81E9
Median fraction of KE loss (%)	70	83	52
Interquartile range (%)	65 - 79	75 - 90	43 - 61
Median total impactor momentum (cluster) (Ns)	260000	-	-
Interquartile range	198000 - 340000	-	-

(Ns)			
Median total vertical impactor momentum (cluster) (Ns)	100000	-	-
Interquartile range (Ns)	77000 - 131000	-	-
Median total pre-entry mass (cluster) (kg)	186	-	-
Interquartile range (kg)	150-237	-	-
Median main fragmentation altitude (km)	16.8	-	-
Interquartile range (km)	12.9 - 21.0	-	-
Median total energy deposited in air (J)	8.3E+09	-	-
Interquartile range (J)	4.7E9 - 1.4E10	-	-

Tab. 3| Estimates of the seismic source parameters and impact parameters
Seismic moment is obtained by scaling the first arrival P wave amplitude to numerical simulations with seismic quality factors ranging from 100 to 2000.
Impactor parameters are estimated for the meteoroid fragment(s) that produced the largest crater in the cluster and for the entire meteoroid that produced all craters in the cluster (cluster). Parameters for single (largest) craters are derived from statistical model of atmospheric entry of meteoroids[27]; cluster parameters are derived from supplementary atmospheric entry simulations, which used the inferred approximate trajectory angle of the meteoroid, as well as the effective diameter of the cluster, the observed number of craters, the median separation distance between craters and the aspect ratio of the best-fitting ellipse, to constrain the impact scenario.

Figures (<3 and legends <200 words):

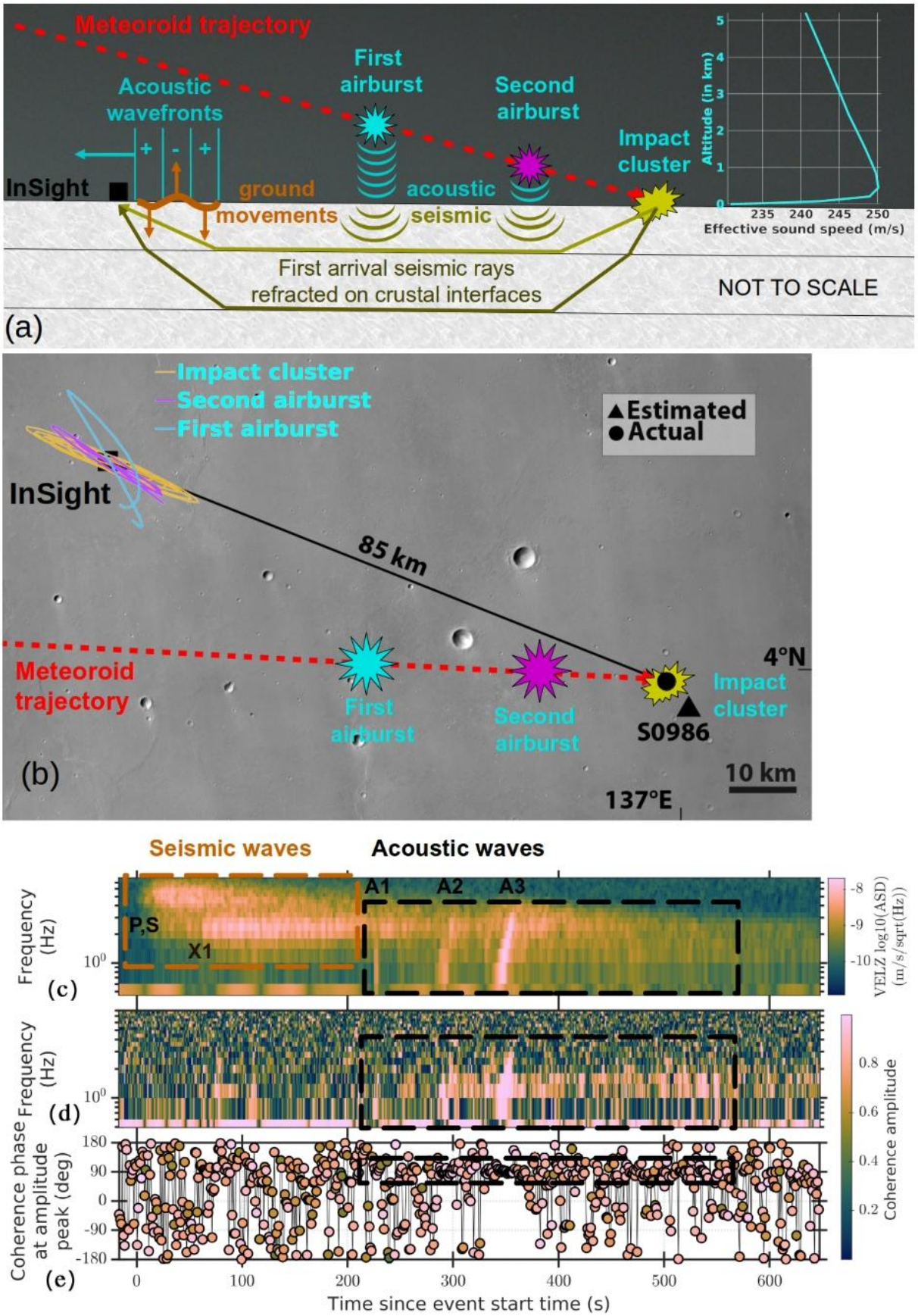

Fig. 1| Sketch of meteor impact phenomena and their recordings by InSight

a, Sketch of physical processes during meteoroid entry and impact, and effective sound speed profile from impact direction to InSight extracted from Mars Climate Database. Labels in parentheses locate the sources of the main acoustic and seismic arrivals. **b**, Impact location and estimated meteoroid entry path on CTX mosaic background. Polarization of main acoustic signals is depicted at InSight location. **c**, spectrogram of vertical component of ground velocity for S0986c seismic event, showing the three main seismic arrivals (P, S, X1) and the three main acoustic arrivals (A1, A2, A3). P, S, and A3 are associated with the impact source, and X1, A1, and A2 with the two airbursts. **d**, coherence as a function of time and frequency and **e**, phase relation between vertical and horizontal ground velocities at maximum coherence value. Times are provided relative to Event Start time (2021-09-05 05:23:58.00 UTC).

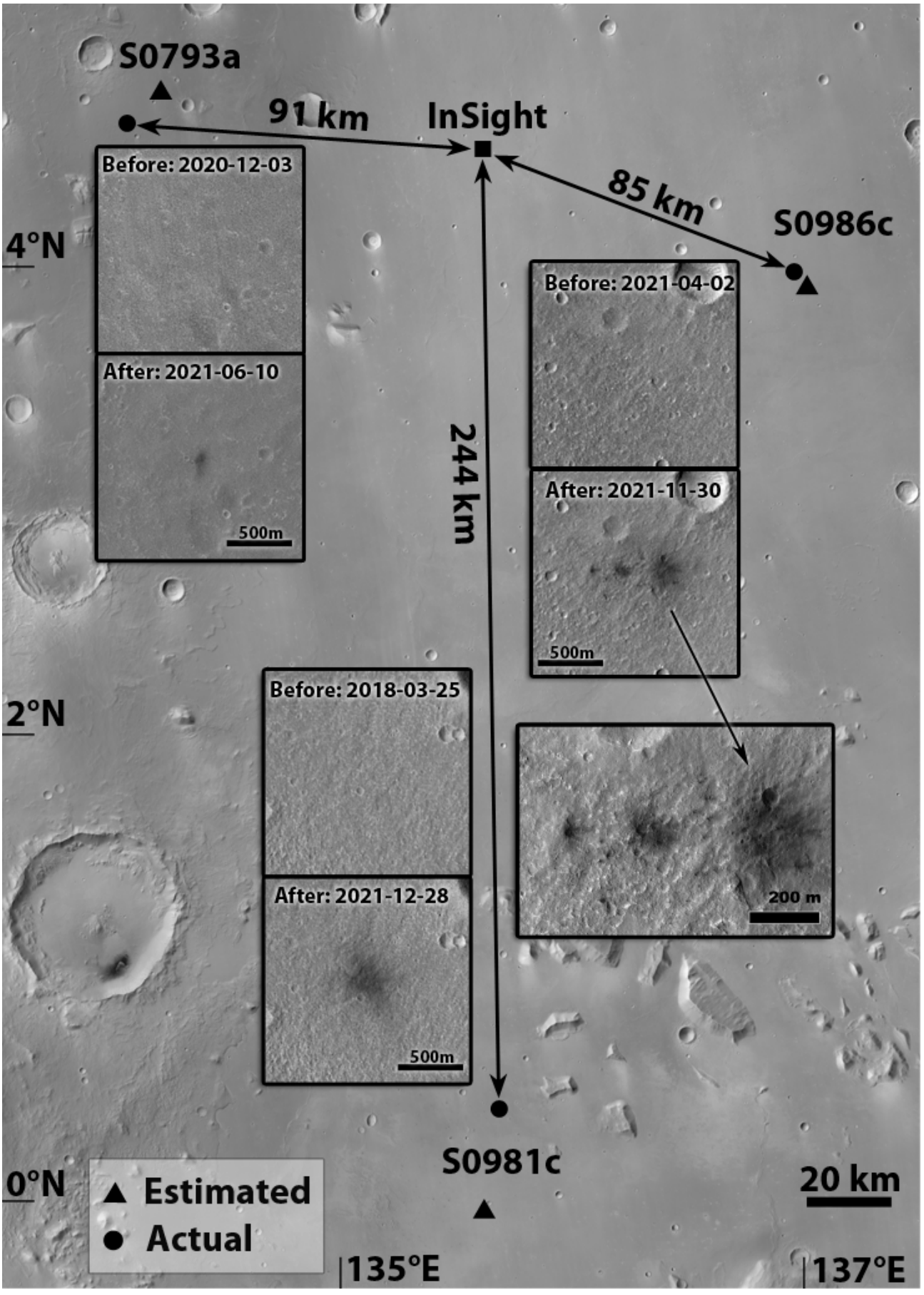

Fig. 2| Impacts observed from orbit
Locations of three new impact sites as estimated from the seismic data (triangles) and actual impacts (circles) imaged by Mars Reconnaissance Orbiter instruments showing

before and after details of CTX images on CTX mosaic background. For the S0986c associated event, a detailed view by HiRISE is also shown. Image credits: NASA/JPL/MSSS/U Arizona.

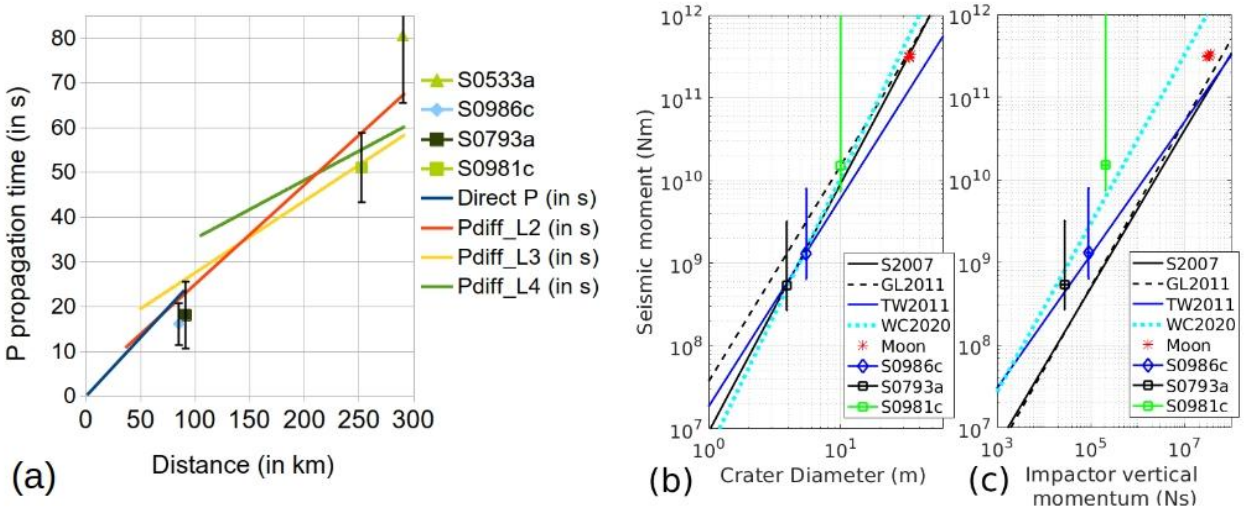

Fig. 3| Crust structure and impact seismic sources
a, P wave propagation time (in s) as a function of propagation distance (in km) for the three impact events, and seismic direct and head waves propagation times predicted by reference model KKS21_GP [5.0,5.1]. Data are presented as best values +/- SEM. **b, c,** Seismic moment (in Nm) as a function of crater diameter (in m) and Impactor vertical momentum (in Ns) estimated for the three observed impacts (S0986c, S0793a and S0981c), for Lunar artificial impacts [34,41], and for various impact/seismic models [42, 35, 43, 39]. Data are presented as a best value estimated from simulations with a quality factor of 2000. The error bar covers the range of estimates obtained with quality factors ranging from 100 to 2000. On the lower side of the estimates a 50% error is added to take into account uncertainties on other parameters that modify the body wave amplitudes.

References (<40):

1- Tauzin, B., Debayle, E., Quantin, C., & Coltice, N. Seismoacoustic coupling induced by the breakup of the 15 February 2013 Chelyabinsk meteor. *Geophysical Research Letters*, **40**(14), 3522-3526 (2013). https://doi.org/10.1002/grl.50683

2- Neidhart, T., Miljković, K., Sansom, E. K., Devillepoix, H. A. R., Kawamura, T., Dimech, J. L., et al. Statistical analysis of fireballs: Seismic signature survey. *Publications of the Astronomical Society of Australia*, **38**, e016 (2021). https://doi.org/10.1017/pasa.2021.11

3- Whipple, F.J.W. The great Siberian meteor and the waves, seismic and aerial, which it produced. *Q. J. R. Meteorol. Soc.* **56**, 287–304 (1930)

4- Le Pichon A. et al. Evidence for a meteoritic origin of the September 15, 2007, Carancas crater. *Meteorit. Planet. Sci.* **43**, 1797–1809 (2008). https://doi.org/10.1111/j.1945-5100.2008.tb00644.x

5- McGarr, A., Latham, G. V., & Gault, D. E. Meteoroid impacts as sources of seismicity on the Moon. *Journal of Geophysical Research*, ***74***(25), 5981-5994 (1969). https://doi.org/10.1029/JB074i025p05981

6- Oberst, J., & Nakamura, Y. Distinct meteoroid families identified on the lunar seismograms. *Journal of Geophysical Research: Solid Earth*, ***92***(B4), E769-E773 (1987). https://doi.org/10.1029/JB092iB04p0E769

7- Lognonné, P. H. & Banerdt, W. B. & Giardini, D. & Pike, W. T. & Christensen, U. & Laudet, P. & et al. SEIS: Insight's Seismic Experiment for Internal Structure of Mars. *Space Science Reviews*, **215** (1), 1-12 (2019). https://doi.org/10.1007/s11214-018-0574-6

8- Spiga, A., Banfield, D., Teanby, N. A., Forget, F., Lucas, A., Kenda, B., ... & Banerdt, W. B. Atmospheric science with InSight. *Space Science Reviews*, **214**(7), 1-64 (2018). https://doi.org/10.1007/s11214-018-0543-0

9- Banfield, D., Rodriguez-Manfredi, J. A., Russell, C. T., Rowe, K. M., Leneman, D., Lai, H. R., ... & Banerdt, W. B. InSight auxiliary payload sensor suite (APSS). *Space Science Reviews*, **215**(1), 1-33 (2019). https://doi.org/10.1007/s11214-018-0570-x

10- Banerdt, W. B., Smrekar, S. E., Banfield, D., Giardini, D., Golombek, M., Johnson, C. L., ... & Wieczorek, M. Initial results from the InSight mission on Mars. *Nature Geoscience*, **13**(3), 183-189 (2020). https://doi.org/10.1038/s41561-020-0544-y

11- Daubar, I., Lognonné, P., Teanby, N. A., Miljkovic, K., Stevanović, J., Vaubaillon, J., et al. Impact-seismic investigations of the InSight mission. *Space Science Reviews*, **214**(8), 1-68 (2018). https://doi.org/10.1007/s11214-018-0562-x

12-Ceplecha, Z., Borovička, J., Elford, W. G., ReVelle, D. O., Hawkes, R. L., Porubčan, V., & Šimek, M. Meteor phenomena and bodies. *Space Science Reviews*, **84**(3), 327-471 (1998). https://doi.org/10.1023/A:1005069928850

13- Edwards, W. N., Eaton, D. W., & Brown, P. G. (2008). Seismic observations of meteors: Coupling theory and observations. *Reviews of Geophysics*, **46**(4), 2007RG000253 (2008). https://doi.org/10.1029/2007RG000253

14-Stevanović, J., Teanby, N. A., Wookey, J., Selby, N., Daubar, I. J., Vaubaillon, J., & Garcia, R. Bolide airbursts as a seismic source for the 2018 Mars InSight mission. *Space Science Reviews*, **211**(1), 525-545 (2017). https://doi.org/10.1007/s11214-016-0327-3

15- Garcia, R.F. & Brissaud, Q. & Rolland, L.M. & Martin, R. & Komatitsch, D. & Spiga, A., et al. Finite-difference modeling of acoustic and gravity wave propagation in Mars atmosphere: Application to infrasounds emitted by meteor impacts. *Space Science Reviews* **211**(1-4), 547–570 (2017). https://doi.org/10.1007/s11214-016-0324-6

16- Herrin, E. T. & Kim, T. S. & Stump, B. W. Evidence for an infrasound waveguide. *Geophysical Research Letters*, **33**, L07815 (2006). https://doi.org/10.1029/2005GL025491

17- Negraru, P. T., & Herrin, E. T. (2009). On Infrasound Waveguides and Dispersion. *Seismological Research Letters*, **80**(4), 565–571 (2009). https://doi.org/10.1785/gssrl.80.4.565

18- InSight Marsquake Service (2022). Mars Seismic Catalogue, InSight Mission; V9 2022-01-01. ETHZ, IPGP, JPL, ICL, Univ. Bristol. https://doi.org/10.12686/a14

19- Clinton, J. F., Ceylan, S., van Driel, M., Giardini, D., Stähler, S. C., Böse, M., ... & Stott, A. E. The Marsquake catalogue from InSight, sols 0–478. *Physics of the Earth and Planetary Interiors*, **310**, 106595, (2021). https://doi.org/10.1016/j.pepi.2020.106597

20- Martire, L. & Garcia, R. F. & Rolland, L. & Spiga, A. & Lognonné, P. H. & Banfield, D. & Banerdt, W.B. & Martin, R. Martian infrasound: Numerical modeling and analysis of InSight's data. *Journal of Geophysical Research: Planets*, ***125***(6), e2020JE006376 (2020). https://doi.org/10.1029/2020JE006376

21- Sorrells, G.G. A preliminary investigation into the relationship between long period seismic noise and local fluctuations in the atmospheric pressure field. *Geophysical Journal of the Royal Astronomical Society*, **26**(1-4), 71–82 (1971). https://doi.org/10.1111/j.1365-246X.1971.tb03383.x

22- Schneider, F.M, F. Fuchs, P.Kolínsky, E.Caffagni, S.Serafin, M.Dorninger, G. Bokelmann,AlpArray Working Group, Seismo-acoustic signals of the Baumgarten (Austria) gas explosion detected by the AlpArray seismic network, Earth and Planetary Science Letters, 502, 104-114 (2018). https://doi.org/10.1016/j.epsl.2018.08.034

23- Millour, E. & Forget, F. & González-Galindo, F. & Spiga, A. & Lebonnois, S. & Lewis, S. R., et al. The Mars Climate Database (version 5.3). *Sae technical paper series 2*. (2018)

24- Malin, M. C., Bell, J. F., Cantor, B. A., Caplinger, M. a., Calvin, W. M., Clancy, R. T., et al. Context Camera Investigation on board the Mars Reconnaissance Orbiter. *Journal of Geophysical Research*, **112**(E5), E05S04 (2007). https://doi.org/10.1029/2006JE002808

25- Daubar, I. J., McEwen, A. S., Byrne, S., Kennedy, M. R., & Ivanov, B. A. The current martian cratering rate. *Icarus*, **225**(1), 506–516 (2013). https://doi.org/10.1016/j.icarus.2013.04.009

26- McEwen, A. S., Tornabene, L. L., Eliason, E. M., Bergstrom, J. W., Bridges, N. T., et al. Mars Reconnaissance Orbiter's High Resolution Imaging Science Experiment (HiRISE). *Journal of Geophysical Research*, **112**(E5), E05S02 (2007). https://doi.org/10.1029/2005JE002605

27- Collins, G. S., Newland, E. L., Schwarz, D., Coleman, M., McMullan, S., Daubar, I. J., et al. (2022). Meteoroid fragmentation in the martian atmosphere and the formation of crater clusters. *Journal of Geophysical Research: Planets*, *127*, e2021JE007149. https://doi.org/10.1029/2021JE007149

28- Knapmeyer-Endrun, B., Panning, M. P., Bissig, F., Joshi, R., Khan, A., Kim, D., ... & Banerdt, W. B. Thickness and structure of the martian crust from InSight seismic data. *Science*, **373**(6553), 438-443 (2021). https://doi.org/10.1126/science.abf8966

29- Stähler, S. C. & Khan, A. & Banerdt, W. B. & Lognonné & P., Giardini & D., Ceylan, S. et al. Seismic detection of the martian core. *Science*, **373**(6553), 443-448 (2021). https://doi.org/10.1126/science.abi7730

30- Daubar, I. J., McEwen, A. S., Byrne, S., Kennedy, M. R., & Ivanov, B. A. The current martian cratering rate. *Icarus*, **225**(1), 506–516 (2013). https://doi.org/10.1016/j.icarus.2013.04.009

31- Bland, P. A., & Artemeiva, N. A. The rate of small impacts on Earth. *Meteoritics & Planetary Science*, *41*(4), 607–631 (2006). https://doi.org/10.1111/j.1945-5100.2006.tb00485.x

32- Daubar, I., Lognonné, P., Teanby, N.A., Miljkovic, K., Stevanović, J., Vaubaillon, J., Kenda, B., Kawamura, T., Clinton, J., Lucas, A., Drilleau, M., Yana, C., Collins, G.S., Banfield, D., Golombek, M., Kedar, S., Schmerr, N., Garcia, R., Rodriguez, S., Gudkova, T., May, S., Banks, M., Maki, J., Sansom, E., Karakostas, F., Panning, M., Fuji, N., Wookey, J., van Driel, M., Lemmon, M., Ansan, V., Böse, M., Stähler, S., Kanamori, H., Richardson, J., Smrekar, S., Banerdt, W.B., Impact-Seismic Investigations of the InSight Mission. *Space Sci. Rev.* **214**, 132 (2018). https://doi.org/10.1007/s11214-018-0562-x

33- Daubar, I.J., Lognonné, P., Teanby, N.A., Collins, G.S., Clinton, J., Stähler, S., Spiga, A., Karakostas, F., Ceylan, S., Malin, M., McEwen, A.S., Maguire, R., Charalambous, C., Onodera, K., Lucas, A., Rolland, L., Vaubaillon, J., Kawamura, T., Böse, M., Horleston, A., van Driel, M., Stevanović, J., Miljković, K., Fernando, B., Huang, Q., Giardini, D., Larmat, C.S., Leng, K., Rajšić, A., Schmerr, N., Wójcicka, N., Pike, T., Wookey, J., Rodriguez, S., Garcia, R., Banks, M.E., Margerin, L., Posiolova, L., Banerdt, B. A New Crater Near InSight: Implications for Seismic Impact Detectability on Mars. *Journal of Geophysical Research: Planets* **125**, e2020JE006382 (2020). https://doi.org/10.1029/2020JE006382

34- Lognonné, P., Le Feuvre, M., Johnson, C.L., Weber, R.C., Moon meteoritic seismic hum: steady state prediction. *J. Geophys. Res.* **114**, E12003 (2009) https://doi.org/10.1029/2008JE003294

35- Gudkova, T., Lognonné, P., Miljković, K., & Gagnepain-Beyneix, J. Impact cutoff frequency – momentum scaling law inverted from Apollo seismic data. *Earth and Planetary Science Letters*, **427**, 57–65 (2015). https://doi.org/10.1016/j.epsl.2015.06.037

36- Martire, L. & Martin, R. & Brissaud, Q. & Garcia, R. F. SPECFEM2D-DG, an open-source software modelling mechanical waves in coupled solid–fluid systems: the linearized Navier–Stokes approach. *Geophysical Journal International*, **228**(1), 664-697 (2022). https://doi.org/10.1093/GJI/GGAB308

37- Schmerr, N. C., Banks, M. E., & Daubar, I. J. The Seismic Signatures of Recently Formed Impact Craters on Mars. *Journal of Geophysical Research: Planets*, **124**(11), 3063–3081 (2019). https://doi.org/10.1029/2019JE006044

38- Lognonné, P., W.B. Banerdt, W.T.Pike, D.Giardini, U.Christensen, R.F.Garcia,T.Kawamura, S.Kedar, B. Knapmeyer-Endrun, L.Margerin, F.Nimmo, M.Panning, B.Tauzin, J.-R.Scholz, D.Antonangeli, S.Barkaoui, E.Beucler, F. Bissig, N. Brinkman, M. Calvet, S,Ceylan, C.Charalambous, P.Davis, M. van Driel, M.Drilleau, L.Fayon, R. Joshi, B.Kenda, A. Khan, M. Knapmeyer, V. Lekic, J.McClean, D.Mimoun, N.Murdoch, L. Pan, C.Perrin, B.Pinot, L.Pou, S. Menina, S.Rodriguez, C. Schmelzbach, N. Schmerr, D. Sollberger, A.Spiga, S.Stähler, A.Stott, E.Stutzmann, S.Tharimena, R.Widmer-Schnidrig, F. Andersson, V.Ansan, C. Beghein, M.Böse),E. Bozdag, J. Clinton, I.Daubar, P.Delage, N. Fuji, M. Golombek, M. Grott, A. Horleston, K. Hurst, J. Irving, A. Jacob, J. Knollenberg, S.Krasner, C. Krause, R. Lorenz, C. Michaut, B.Myhill, T. Nissen-Meyer, J. ten Pierick, A.-C..Plesa, C.Quantin-Nataf, J.Robertsson, L. Rochas, M.Schimmel, S.Smrekar, T.Spohn, N.Teanby, J.Tromp, J.Vallade, N.Verdier, C.Vrettos, R. Weber, D.Banfield, E. Barrett, M.Bierwirth, S.Calcutt, N.Compaire, C.Johnson, D.Mance, F. Euchner, L.Kerjean, G.Mainsant, A.Mocquet, J.Antonio Rodriguez Manfredi, G.Pont, P.Laudet, T.Nebut, S. de Raucourt, O. Robert, C.T. Russell, A.Sylvestre-Baron, S.Tillier, T.Warren, M.Wieczorek, C.Yana, P.Zweifel, Constraints on the shallow elastic and anelastic structure of Mars from InSight seismic data, *Nature geoscience*, **13**, 213-220, (2020) doi: 10.1038/s41561-020-0536-y

39- Wójcicka, N., Collins, G. S., Bastow, I. D., Teanby, N. A., Miljković, K., Rajšić, A., Daubar, I., & Lognonné, P. The Seismic Moment and Seismic Efficiency of Small Impacts on Mars. *Journal of Geophysical Research: Planets*, **125**(10), e2020JE006540 (2020). https://doi.org/10.1029/2020JE006540

40- Teanby, N. A. Predicted detection rates of regional-scale meteorite impacts on Mars with the InSight short-period seismometer. *Icarus*, **256**, 49–62 (2015). https://doi.org/10.1016/j.icarus.2015.04.012

41- J.B. Plescia J.B., Robinson M.S.S., Wagner, R. Baldridge R., Ranger and Apollo S-IVB spacecraft impact craters. *Planet. Space Sci.* **124**, 15–35 (2016). https://doi.org/10.1016/j.pss.2016.01.002

42- Shishkin N.I., Seismic efficiency of a contact explosion and a high-velocity impact. J. Appl. Mech. Tech.Phys. **48**, 145–152 (2007). https://doi.org/10.1007/s10808-007-0019-6

43- Teanby N.A., Wookey J., Seismic detection of meteorite impacts on Mars. *Phys. Earth Planet. Inter.* **186**, 70–80 (2011). https://doi.org/10.1016/j.pepi.2011.03.004

Methods (<3000 words):

The seismic events discussed in this study were detected by the Marsquake Service (MQS) and classified as Very High Frequency (VF) events [44,18] by using data from the Very Broad Band (VBB) sensors of the SEIS instrument [7]. These data have been corrected for "tick noise" and "glitch" artifacts using published methods [45,46]. No InSight wind or pressure data are available at the time of the seismic events discussed in this study, except for the S0533a event. The VF events, by definition, consist of signals with high frequency energy predominantly above 2.4 Hz and with particularly high amplitude energy on the horizontal components between 6 and 10 Hz [47,19].

Events S0793a, S0981c, S0986c and S0533a differ from all other VF events due to the presence of a short duration dispersed wavetrain recorded by the SEIS VBB sensors between 250 and 1000 seconds after the first arrival (**Extended data Fig. 1-3**). These dispersed wavetrains share the following characteristics for all four events: frequencies in the range 0.4 to 4 Hz, low frequencies arriving before high frequencies, signals strongly polarized in a given horizontal direction, and a strong coherency between the vertical and horizontal components along the polarization direction. The P, S, and acoustic signal arrival times used for estimating the impact locations are a median value taken from arrival times provided by three different research teams inside the InSight science team, and by the MQS. The standard deviation between these estimates is used as a proxy to estimate the error on the location parameters. The MQS assigns a magnitude to VF events that is based on the amplitude of the peak energy at 2.4 Hz, $M_{2.4Hz,spec}^{Ma}$ [48]. These magnitudes are 1.4, 1.6, 1.2 and 2.3 for S0793a, S0981c, S0986c and S0533a, respectively. Note these magnitudes are based on the MQS estimate of epicentral distance, which is different for these events than the one observed by crater imaging (S0793a: 178 vs 84 km; S0981c: 204 vs 269 km; S0986c: 72 vs 86 km; S0533a: 322 vs 244 km). The calibration between moment magnitude and seismic moment is only valid at distances greater than 150 km, since at the time of the study, the catalog did not include any closer events.

Due to power restrictions on InSight operations, the meteorological sensors of the Auxiliary Payload Sensor Suite (APSS) were not acquiring data during these events, except during the S0533a event. Nevertheless, owing to the high level of atmospheric repeatability in non-dusty Martian seasons like those considered here [8], wind amplitude and pressure perturbations expected during these events can be assessed by InSight meteorological data acquired at the corresponding sols in the previous Martian year; three-sol averages of such diagnostics denote near-surface low-amplitude nighttime southwesterly [i.e. coming from the southwest] winds for all events. This technique, inspired by previous missions to Mars, is confirmed by comparing InSight atmospheric data available for two successive Martian years. The low-amplitude southwesterly regime is also confirmed by afternoon APSS data acquired prior to the S0981c and S0986c events, at the same season, on sol 965, as well as from 20 minutes after the S0793a event to midnight.

Global climate models reproduce the near-surface southwesterly wind regime detected by InSight at the season of the considered events i.e. northern spring/summer [8,9] and, given their validation upon infrared atmospheric profiling on board Mars Reconnaissance Orbiter [23], can be used to derive the vertical profiles of temperature and winds to assess atmospheric wave propagation [15]. Global climate model results compiled in monthly climatologies in the Mars Climate Database (MCD) version 5.3 [23] were used in this work by all the atmospheric modeling tools presented (**Extended Data Fig. 4-5-6**). The variations in acoustic waveguide properties are due to both air temperature variations, as a

function of local time, and projected wind variations, as a function of wave propagation direction.

We use WASP-3D software to simulate the 3D propagation of acoustic waves emitted by a source in a stratified and windy atmosphere [49]. These simulations assess the presence of ducts capable of turning back the acoustic energy toward the ground, and the back azimuth deviations induced by cross winds. In all simulated cases, we can see the multiple rebounds of acoustic rays in the thin low atmosphere duct. Cross winds deviate all the simulated rays by less than 5° relative to their direction at the source. The remaining acoustic energy escapes upward in totality, except for event S0986c, for which a part of the remaining acoustic energy is turned back toward the ground by thermospheric winds at distances larger than 200 km (**Extended Data Fig. 4**). Atmospheric explosions are also simulated. The rays follow an almost straight line trajectory to InSight, and no secondary arrivals are predicted from thermosphere wind ducts.

The conversion factor from acoustic pressure waves to ground velocity cannot be inferred from the data in the absence of measurements from the pressure sensor. However, the pressure sensor was recording during event S0533a. Unfortunately, due to the high environment noise at that time of the day, the pressure perturbations induced by the infrasounds were not observed. However, from the amplitude of background pressure we can estimate a lower bound for the vertical compliance at 1 Hz equal to 4e-7 m/s/Pa. This value is consistent with a recent estimate of 6e-7 m/s/Pa at 1 Hz frequency [50]. As a consequence, the guided acoustic waves described here are expected to have an amplitude between 1.5 and 45 mPa in the 0.5-1.5 Hz range.

The various acoustic and seismic sources of the impact events are modeled by the SPECFEM2D-DG software [36]. This open-source software relies on recent developments of mechanical wave propagation in the coupled solid/atmosphere system [51]. These simulations couple acoustic and gravity waves in realistic atmosphere models to the SPECFEM code modeling the propagation of elastic waves in the solid part of the planet [52]. Concerning the application to Martian seismic and acoustic waves, the software includes winds and attenuation of acoustic waves, including the strong attenuation by carbon dioxide vibration modes [8]. The modeling tool intrinsically incorporates compliance effects induced by propagating pressure perturbations in the atmosphere [20]. The atmosphere models used are extracted from Mars Climate Database (**Supplementary Information Fig. 2**). The internal structure model is the model KKS21_GP, on top of which a sedimentary layer of 100 m thickness is added with the following seismic properties: density = 1800 kg/m³, P velocity = 744 m/s, S velocity = 398 m/s. This layer is set according to the sub-surface properties determined from the inversion of compliance values [53], and it produces an acoustic compliance of 2e-7 m/s/Pa at 1Hz. Two different seismic quality factor values are tested (100 and 2000) to investigate their effect on the seismic moment estimates.
The seismic and acoustic sources are produced by using a gaussian source time function model of, respectively, 8 Hz and 3 Hz dominant frequency. The seismic source is simulated with an isotropic moment tensor. The acoustic sources are simulated with an energy term. Each source is simulated in a different computation and the resulting synthetic ground velocities are summed. The scattered seismic and acoustic waves cannot be reproduced with homogeneous models such as these.
For the event S0986c, the altitude of the source of airburst A2 is determined by measuring the differential time between the X1 and P wave arrivals, and assuming that the X1 seismic signals propagate at P wave speed and are created by acoustic waves converted

into seismic waves below the airburst position. This computation, when combined with the knowledge of the incoming back azimuth from infrasound polarization, provides airburst altitudes in the range 13-16 km. Then, by fitting the A2 arrival waveform for a source altitude of 15 km, a horizontal distance from InSight of 71 km is estimated for the A2 airburst. From these estimates, an impact angle of 30°±8° is estimated. Eventually, the position of the A1 airburst is estimated to be at 26 km altitude and 48 km horizontal distance from InSight, by using the impact angle and the polarization direction of the A1 infrasounds.
As a consequence, we present the synthetic SEIS waveforms that reproduce the main seismic (P, S, X1) and acoustic (A1, A2, A3) arrivals at the proper times and with the proper dispersion up to 2 Hz (**Extended Data Fig. 5**) by using two airburst sources (A1 and A2), respectively, at 26 km and 15 km altitude, and 48 km and 71 km horizontal distance from InSight. Other positions are also possible due to uncertainties in polarization directions and a trade-off between distance and altitude. The synthetic acoustic signal from A2 is not as dispersive as the one observed in the data. We ascribe this difference to the scattering of A2 acoustic waves by either heterogeneities in the atmosphere or surface topography that is exciting the low atmosphere waveguide. These effects are not modeled in our simulations.
The dispersed acoustic wave from the impact cluster is simulated by using 3 sources at 87 km distance separated by 1 second in time with decreasing energy ratios by factors 1, 1/10 and 1/20. The amplitude scaling of the simulated records of acoustic wave trains in the 0.5-1.5 Hz range, and first arrival P waves in the 3-8 Hz range, allows us to provide estimates of airburst energy and impact seismic moment after correcting for geometrical spreading differences between 2D simulations and 3D real data [54] (**Tab. 2, Tab. 3)**. However, because the compliance value in the simulations is three times less than our best estimates, the yield values from the simulations are divided by a factor of 3 in order to be consistent with our knowledge of acoustic compliance. For the seismic moment estimates, results are provided for seismic quality factor values of 100 and 2000 in the crust. The overestimate of the seismic moment of the most distant event S0981c relative to the estimates from vertical impact momentum (**Fig. 3c**) suggest that the seismic quality factor is larger than 2000 in the 3-8 Hz range, as previously inferred from the analysis of the seismic codas [56].

We compute the group velocities of guided acoustic waves using the atmosphere models previously described. This computation is performed by using the propagation matrix method used in the calculation of Love-wave dispersion in seismology [57]. A strong dispersion is predicted in the 0.5-4 Hz frequency range (**Extended Data Fig. 6**). In order to fit the measured dispersion with our synthetic results, we correct the atmosphere models from a constant wind speed of less than 10 m/s. After this correction, the synthetic and measured dispersions agree well with each other, thus validating the shape of the atmosphere waveguide. In addition, the eigenfunctions indicate that the guided wave trains above 1.5 Hz can only be excited by sources below 1500 m altitude. This modeling is consistent with the observation of weakly dispersed wave trains for high altitude airburst sources during the S0986c event.

An important parameter for interpreting and scaling impact-generated seismic waves is impact momentum; however, crater diameter and impact momentum are not uniquely related. To estimate the likely momentum of the meteoroid (fragments) at the ground for each detected event, we leverage previous theoretical and numerical modeling work [11,33,27]. A synthetic dataset of small impact craters on Mars [27], generated by a statistical model of atmospheric entry of meteoroids that is in excellent agreement with the

population of recently observed impact craters, provides constraints on the likely impact parameters. The synthetic dataset was produced by a Monte Carlo simulation of 10,000 stony meteoroid impacts on Mars with mass larger than 15 kg. In each impact simulation, initial properties of the meteoroid were selected at random or according to parameter probability distributions for Mars (e.g., velocity [58] and impact angle [59]). Meteoroid mass was drawn from a distribution based on observations of terrestrial fireballs with mass > 3 kg [60]. Uniform probability distributions were used for stony meteoroid density (1400–4000 kg/m^3) and ablation parameter (1–4.2 x 10^{-8} s^2m^{-2}) [61]. A log-uniform probability distribution for meteoroid strength was used (min. 20 kPa; med. 330 kPa; max. 6 MPa), which produced the best match to the properties of observed clusters and single craters on Mars [27,62].

For the single crater events, S0793a and S0981c, we use this dataset to estimate the pre-entry mass, as well as the momentum, mass, speed, and trajectory angle to the horizontal of the meteoroid at the ground (**Tab. 3**) based on the distribution of these values for single craters with a diameter within +/-0.5 m of the observed diameter. For the cluster-forming impact S0986c, we estimate the momentum, mass and velocity of the largest fragment in a similar way from the existing synthetic dataset, with the additional constraint that the impact angle at the ground was approximately 30 degrees, based on the inferred approximate trajectory angle of the meteoroid. To further investigate impact scenarios for event S0986c, a supplementary Monte Carlo simulation was performed with a minimum mass of 100 kg and a range of impact angle of 20-40 degrees. All other parameter distributions were the same as the published dataset. Candidate scenarios were selected from the new synthetic data set based on effective diameter of the cluster, number of craters, median separation distance between craters, and aspect ratio of the best-fitting ellipse. This allowed us to estimate the total impactor momentum (all impacting fragments), the total pre-entry meteoroid mass, and the total energy deposited in the atmosphere. We also determined the main break-up altitude for each impact that produced a cluster consistent with observations. The outcome of an example simulation of meteoroid entry that is consistent with event S0986c is shown in **Extended Data Fig. 7**.

Our results (**Tab. 3**) indicate that the detected events involved meteoroids with a pre-entry mass of 20-200 kg, which underwent substantial deceleration and ablation during atmospheric entry, resulting in >50% loss of kinetic energy. It is this rapid energy deposition that generated the strong, polarized acoustic wave signal that is a hallmark of the impact-generated seismic signals detected on Mars. Such dramatic deceleration is consistent with previous atmospheric entry modeling of small meteoroids on Mars [62,63]. For single-crater events, energy loss is a continuous result of ablation and drag; for cluster-forming events, additional energy is lost by each major fragmentation event owing to the instantaneous increase in drag with increase in surface area. For the cluster-forming event, S0986c, the inferred airburst altitude of 13-16 km is very consistent with the main break-up altitudes from atmospheric entry modeling (interquartile range 12.9-21.0 km). Moreover, estimates of total energy deposition in the atmosphere of 4.7-14 GJ are consistent with full waveform models of the seismic signal for S0986c that invoke between 0.3 and 7.7 GJ energy (point source) airburst events in the atmosphere (**Extended Data Fig. 7**).

To estimate the source cutoff, we analyze the frequency dependency of the P wave packet energy, the latter being computed from spectra on a 5 sec duration window following the P arrival time. **Extended Data Fig. 8** compares results of this analysis for S0793a and S0986c, both at comparable distances. In both cases, an f^3 source mechanism is best fitting the spectra, likely associated to the volumic character of the shock wave as compared to the f^2 spectra of surface faults. The Gudkova model of the source function

[35] is used to fit the spectra, with a cutoff time duration which varies as $Log_{10}(t)=0.14\ Log_{10}(I/I_0)-0.22$, where I is the vertical impulse and I_0 is the reference impulse of 10^7 Ns.. This empirical relationship was fit for observations on the Moon This provides t = 0.35 sec for the impulse of S0986c. Fitting the displacement spectrum with the Gudkova model suggests a smaller value of cutoff time duration of about 0.125 sec. The larger cutoff frequency is likely related to both the larger seismic velocities in the Martian subsurface as compared to the Moon and to the fact that Gudkova et al. 2015 mostly constrained the S wave cutoff instead of the P wave. Another contributing factor is the presence of multiple impacts for S0986c; the smaller impacts, although weaker in amplitude, would extend and modify the shape of energy at the high end of the frequency spectrum [37]. Note, however, that the relative scaling between the S0793a and S0996c cutoffs is compatible with the Gudkova et al. 2015 relationship, with about 9.4 Hz cutoff for the P of S0793a. In both cases, an overshot of the P wave, also observed on the S wave spectra, is likely, as proposed for impact in high porosity materials [11].
Due to attenuation of seismic waves, the source time function of the most distant event (S0981c) cannot be determined without a precise knowledge of seismic attenuation at these frequencies.

In order to compare Martian and Lunar seismic signals from impacts, the envelope of the seismic signal is fit following the methodology used to calibrate seismic signals from artificial impacts on the Moon [34], with a diffusion model [64] depending on the diffusion length scale (s), the epicentral distance (D), the attenuation (q_0), a propagation parameter (a), and a source term (A) proportional to the vertical impulse. For determining the acceptable value, an exploration of the parameters [s, q_0, a] is made, and we compute the L2 residual of the modeled envelope with the observed one. In this process, A is computed by minimizing least squares for a given set of parameters. This first exploration shows that the acceptable fit must have an attenuation parameter q_0 that is significantly smaller for Mars (q_0=2.43) than for the Moon (q_0=3.85).
An example of the data fit is provided for the Martian S0986c impact (**Extended Data Fig. 9a**) compared to the LEM12 impact on the Moon, detected on the Apollo 12 LP vertical seismometer (**Extended Data Fig. 9b**). See [34] for details and [65] for distances of artificial impacts to Lunar stations. A second exploration is made while keeping the attenuation parameter at the value q_0=2.43. In this exploration, the [s, a] parameters are explored over 2 decades around the Lunar values (i.e. 0.1 $s_{Moon} < s_{Mars} < 10\ s_{Moon}$, same for a). For each solution, the source amplitude is then computed and represented as the ratio between the Lunar amplitude requested for modeling the LEM12 impact and the Mars amplitude requested for modeling S0986c. We recall that these amplitudes are proportional to the vertical momentum of the impactors. This impactor ratio A_{Moon}/A_{Mars} is expected to be the impulse ratio for the same propagation parameter, but will integrate the difference in propagation for two planets, with an expected amplification on the Moon due to the lower velocities in the upper Lunar regolith. The acceptable solutions, as function of length scale and of the effective source ratio between the two impactors, are provided for 98% variance reduction (**Extended Data Fig. 9c**). The model parameters for the S0986c impact present a larger attenuation than that found on the Moon. This suggests a larger diffusion length scale on Mars, depending on the strength of the site effects on the Moon as compared to Mars. The latter for force points can be up to 8 when using the velocities at 20 m depth (430 m/s) for Mars [38] as compared to the lower 125 m/s measured on the Moon [66], leading to an effective source ratio up to about 20.

Using the seismic amplitudes and impact momenta estimated above for the three impacts detected by InSight, as well as the data from artificial impacts on the Moon [41,67] (peak

amplitude between 1-16 Hz), and the Carancas impact [68,69], we derive an updated least squares amplitude-distance scaling relationship [39,40], where peak P-wave amplitude (v) is normalized by total impact momentum (p) according to the following power law: $v_{peak} = 1.1 \times 10^{-5}(\frac{p}{10^6 Ns})(\frac{x}{1\ km})^{-1.56}$. This new scaling relationship will be used to update the detectability estimates for impact craters and crater clusters that have been imaged during the InSight mission. **(Extended Data Fig. 10)**.

Data availability

SEIS data are referenced at http://dx.doi.org/10.18715/SEIS.INSIGHT.XB_2016. Orbital imaging data are available in the Planetary Data System (PDS) at https://pds-imaging.jpl.nasa.gov/volumes/mro.html for CTX and https://www.uahirise.org/ for HiRISE. The Mars Climate Database is available at http://www-mars.lmd.jussieu.fr/ The seismic catalog of Mars Quake Service is available at https://science.seis-insight.eu

Code availability

All the computations made in this paper are based on codes described in papers either already published or in revision that are cited in the reference list.
The full wave seismic/acoustic code SPECFEM2D-DG [20] is available at https://github.com/samosa-project/specfem2d-dg. As described in reference [27], for the simulation of meteoroid entry and fragmentation, the implementation of the Separate Fragments Model used here is available at https://github.com/ImperialCollegeLondon/fragmentcloud, and the Monte Carlo code, post-processing code and synthetic data are all available at https://github.com/gsc10/Mars-clusters.

References:

44- Clinton, J., Giardini, D., Böse, M. et al. The Marsquake Service: Securing Daily Analysis of SEIS Data and Building the Martian Seismicity Catalogue for InSight. *Space Sci Rev,* **214**, 133 (2018). https://doi.org/10.1007/s11214-018-0567-5

45- Compaire, N. & Margerin, L. & Garcia, R. F. & Pinot, B. & Calvet & M., Orhand-Mainsant, G. & et al. Autocorrelation of the Ground Vibrations Recorded by the SEIS-InSight Seismometer on Mars. *Journal of Geophysical Research: Planets*, ***126***(4), e2020JE006498 (2021). https://doi.org/10.1029/2020JE006498

46- Scholz, J.-R. &Widmer-Schnidrig, R. & Davis, P. & Lognonné, P. & Pinot, B. & Garcia, R. F. & et al. Detection, analysis, and removal of glitches from InSight's seismic data from mars. *Earth and Space Science*, **7** (11), e2020EA001317 (2020). https://doi.org/10.1029/2020ea001317

47-van Driel, M., Ceylan, S., Clinton, J. F., Giardini, D., Horleston, A., Margerin, L., ... & Banerdt, W. B. High-frequency seismic events on Mars observed by InSight. *Journal of Geophysical Research: Planets*, **126**(2), e2020JE006670 (2021)..

48-Maren Böse, Simon C. Stähler, Nicholas Deichmann, Domenico Giardini, John Clinton, Philippe Lognonné, Savas Ceylan, Martin van Driel, Constantinos Charalambous, Nikolaj Dahmen, Anna Horleston, Taichi Kawamura, Amir Khan, Martin Knapmeyer, Guénolé

Orhand-Mainsant, John-Robert Scholz, Fabian Euchner, W. Bruce Banerdt; Magnitude Scales for Marsquakes Calibrated from InSight Data. *Bulletin of the Seismological Society of America*, **111** (6): 3003–3015 (2021). doi: https://doi.org/10.1785/0120210045

49- Dessa, J. X. & Virieux, J. & Lambotte, S. Infrasound modeling in a spherical heterogeneous atmosphere. *Geophysical Research Letters*, **32** (12), 1–5 (2005). https://doi.org/10.1029/2005GL022867

50- Garcia, R.F & Murdoch, N. & Lorenz, R. & et al. Search for Infrasound Signals in InSight Data Using Coupled Pressure/Ground Deformation Methods. *Bulletin of the Seismological Society of America,* **111** (6), 3055–3064 (2021). https://doi.org/10.1785/0120210079

51- Brissaud, Q. & Martin, R. & Garcia, R. F., & Komatitsch, D. Hybrid Galerkin numerical modelling of elastodynamics and compressible Navier-Stokes couplings: Applications to seismo-gravito acoustic waves. *Geophysical Journal International*, **210** (2), 1047–1069 (2017). https://doi.org/10.1093/gji/ggx185

52- Komatitsch, D., & Vilotte, J.-P. The Spectral Element Method : An Efficient Tool to Simulate the Seismic Response of 2D and 3D Geological Structures. *Bulletin of the Seismological Society of America*, **88** (2), 368–392 (1998). https://doi.org/10.1.1.716.9673

53- Kenda, B. & Drilleau, M. & Garcia, R. F. & Kawamura, T. & Murdoch, N. & Compaire, N. & et al. Subsurface structure at the InSight landing site from compliance measurements by seismic and meteorological experiments. *Journal of Geophysical Research: Planets*, **125**(6), e2020JE006387 (2020). https://doi.org/10.1029/2020JE006387

54- Li, D., Helmberger, D., Clayton, R. W., & Sun, D. Global synthetic seismograms using a 2-D finite-difference method. *Geophysical Journal International*, ***197***(2), 1166-1183 (2014).

55- Glasstone S. The effect of nuclear weapons. *U. S. Atomic Energy Commission*. Washington, D. C. 196–227 (1957).

56- Menina, S., Margerin, L., Kawamura, T., Lognonné, P., Marti, J., Drilleau, M., ... & Banerdt, W. B. Energy Envelope and Attenuation Characteristics of High-Frequency (HF) and Very-High-Frequency (VF) Martian Events. *Bulletin of the Seismological Society of America*, **111**(6), 3016-3034 (2021). https://doi.org/10.1785/0120210127

57- Aki, K., & Richards, P. G. Quantitative Seismology, 2nd Edition (Second ed.). Sausalito, California 94965, USA: University Science Books (2022).

58- Le Feuvre, M., Wieczorek, M.A., 2011. Nonuniform cratering of the Moon and a revised crater chronology of the inner Solar System. Icarus 214, 1–20. https://doi.org/10.1016/j.icarus.2011.03.010

59- Shoemaker, E.M., 1961. Interpretation of Lunar Craters, in: Kopal, Z. (Ed.), Physics and Astronomy of the Moon. Academic Press, pp. 283–359. https://doi.org/10.1016/B978-1-4832-3240-9.50012-2

60- Bland, P.A., Artemieva, N.A., 2006. The rate of small impacts on Earth. Meteoritics & Planetary Science 41, 607–631. https://doi.org/10.1111/j.1945-5100.2006.tb00485.x

61- Britt, D.T., Consolmagno, G.J.S.J., 2003. Stony meteorite porosities and densities: A review of the data through 2001. Meteoritics & Planetary Science 38, 1161–1180. https://doi.org/10.1111/j.1945-5100.2003.tb00305.x

62- Popova, O., Nemtchinov, I., Hartmann, W.K., 2003. Bolides in the present and past martian atmosphere and effects on cratering processes. Meteoritics & Planetary Science 38, 905–925. https://doi.org/10.1111/j.1945-5100.2003.tb00287.x

63- Williams, J.-P., Pathare, A.V., Aharonson, O., 2014. The production of small primary craters on Mars and the Moon. Icarus 235, 23–36. https://doi.org/10.1016/j.icarus.2014.03.011

64- Strobach, K. Scattering of seismic waves and lunar seismograms, *J. Geophys.*, **36**, 643– 645, (1970).

65- Lognonné, P. J.Gagnepain-Beyneix and H. Chenet. A new seismic model of the Moon : implication in terms of structure, formation and evolution, *Earth Plan. Sci. Let.*, **6637**, 1-18, (2003) doi : 10.1016/S0012-821X(03)00172-9

66- Tanimoto, T., Eitzel, M., and Yano, T. The noise cross-correlation approach for Apollo 17 LSPE data: Diurnal change in seismic parameters in shallow lunar crust, *J. Geophys. Res.*, **113**, E08011, (2008) doi:10.1029/2007JE003016

67- Latham, G., Ewing, M., Dorman, J., Press, F., Toksoz, N., Sutton, G., ... & Yates, M. Seismic data from man-made impacts on the Moon. *Science*, **170**(3958), 620-626 (1970).

68- Brown, P., Revelle, D. O., Silber, E. A., Edwards, W. N., Arrowsmith, S., Jackson, L. E., Tancredi, G., & Eaton, D. Analysis of a crater-forming meteorite impact in Peru. *Journal of Geophysical Research*, **113**(E9), E09007 (2008). https://doi.org/10.1029/2008JE003105

69- Kenkmann, T., Artemieva, N. A., Wünnemann, K., Poelchau, M. H., Elbeshausen, D., & Prado, H. N. Del. The Carancas meteorite impact crater, Peru: Geologic surveying and modeling of crater formation and atmospheric passage. *Meteoritics & Planetary Science*, **44**(7), 985–1000 (2009). https://doi.org/10.1111/J.1945-5100.2009.TB00783.X

Extended data

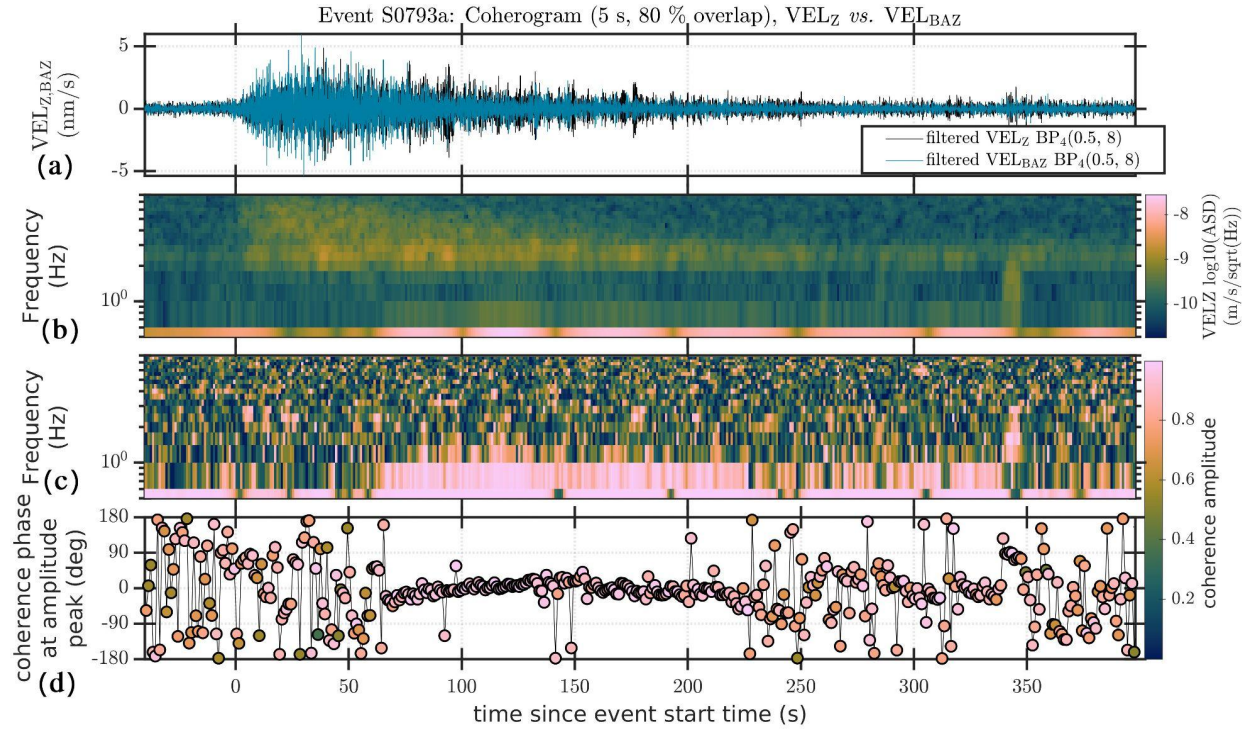

Extended Data Fig. 1| SEIS data of event S0793a
a ground velocity records of vertical and horizontal component in impact direction (280° back azimuth) filtered in the 0.5-8 Hz frequency range. **b** spectrogram of vertical ground velocity. **c** coherence as a function of time and frequency and **d** phase at maximum coherence between vertical and horizontal ground velocity. The low frequency signals with a 0° phase shift between 60 and 250 seconds are due to wind related noise. Times are relative to “Event Start” time (**Tab. 1).**

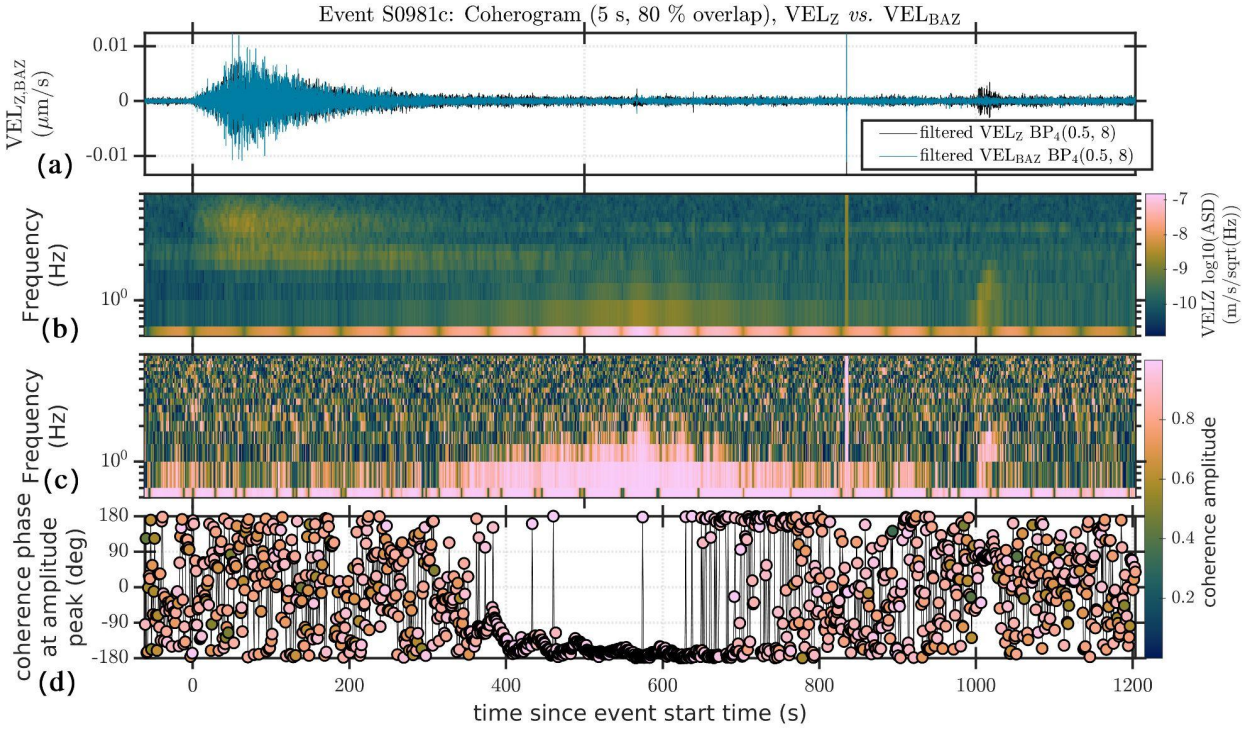

Extended Data Fig. 2| SEIS data of event S0981c

a ground velocity records of vertical and horizontal component in impact direction (180° back azimuth) filtered in the 0.5-8 Hz frequency range. **b** spectrogram of vertical ground velocity. **c** coherence as a function of time and frequency and **d** phase at maximum coherence between vertical and horizontal ground velocity. The low frequency signals with a -170° phase shift between 350 and 800 seconds are due to wind related noise.Times are relative to “Event Start” time (**Tab. 1).**

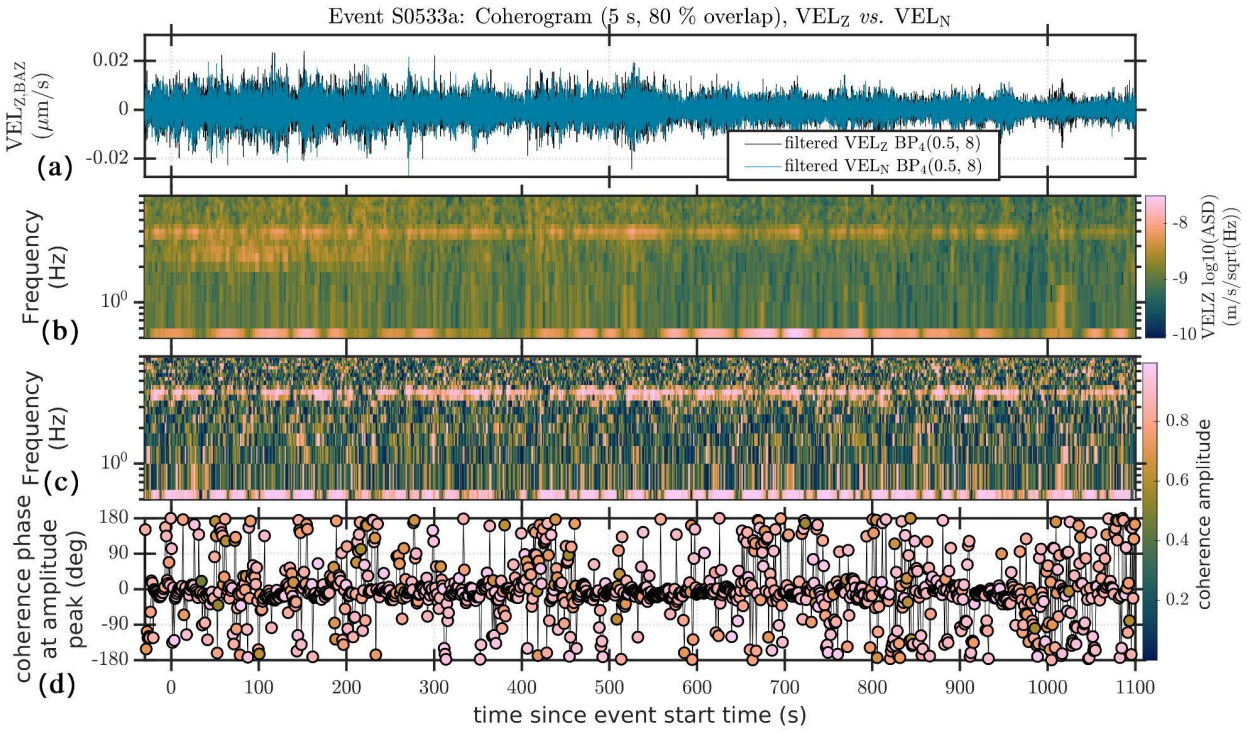

Extended Data Fig. 3| SEIS data of event S0533a
a ground velocity records of vertical and horizontal component in impact direction (0° back azimuth) filtered in the 0.5-8 Hz frequency range. **b** spectrogram of vertical ground velocity. **c** coherence as a function of time and frequency and **d** phase at maximum coherence between vertical and horizontal ground velocity. Times are relative to “Event Start” time (**Tab. 1).**

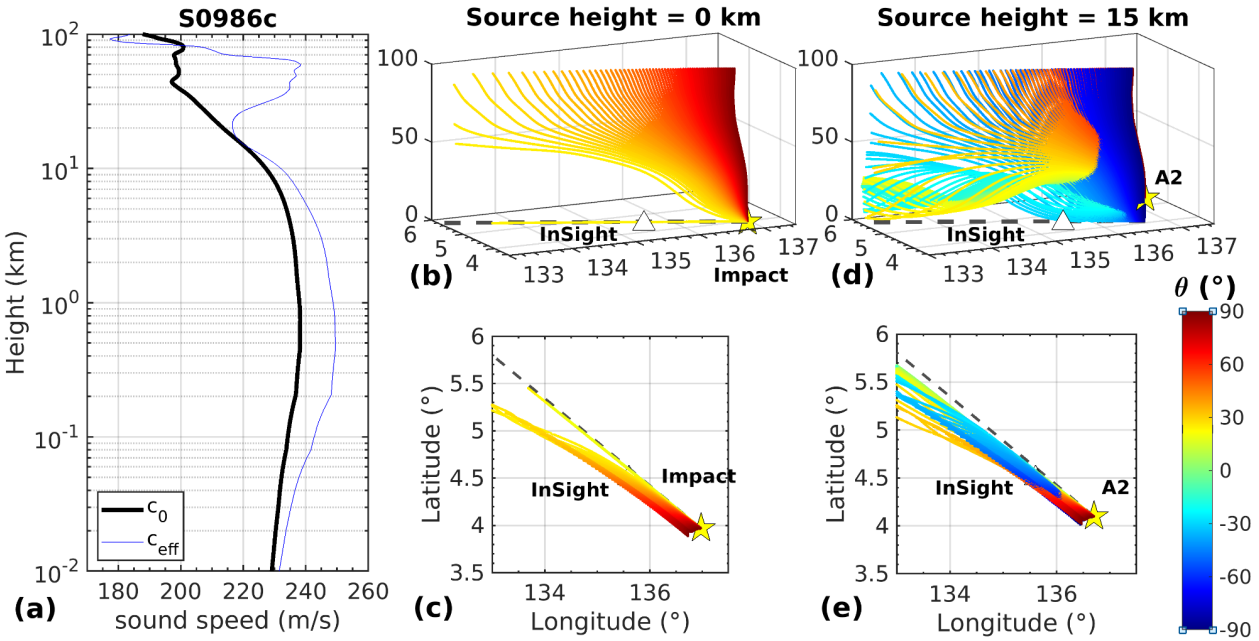

Extended Data Fig. 4| 3D simulation of acoustic rays for S0986c event
a Local sound speed and efficient sound speed profiles from MCD atmospheric model at location and date of S0986c event toward 295° azimuthal direction. **b** Acoustic rays trajectories traced from the impact source and launched with an angle varying from 0° to 90° (see color-code) with a 0.1° step. The impact source and the receiver (InSight station) are marked with a triangle and a star, respectively. We highlight that only acoustic waves trapped close to the surface propagate ground-to-ground. **c** 3D ray tracing top-down view shows that acoustic trapped waves do not deviate from the great circle path highlighted with a dashed grey line. In contrast, the cross-wind effect is visible on upward rays, due to the larger high altitude winds. **d** and **e**: same as **b** and **c**, considering the acoustic source of A2 at 15 km altitude along the meteor trajectory and marked with a star. Downward launch angles are negative.

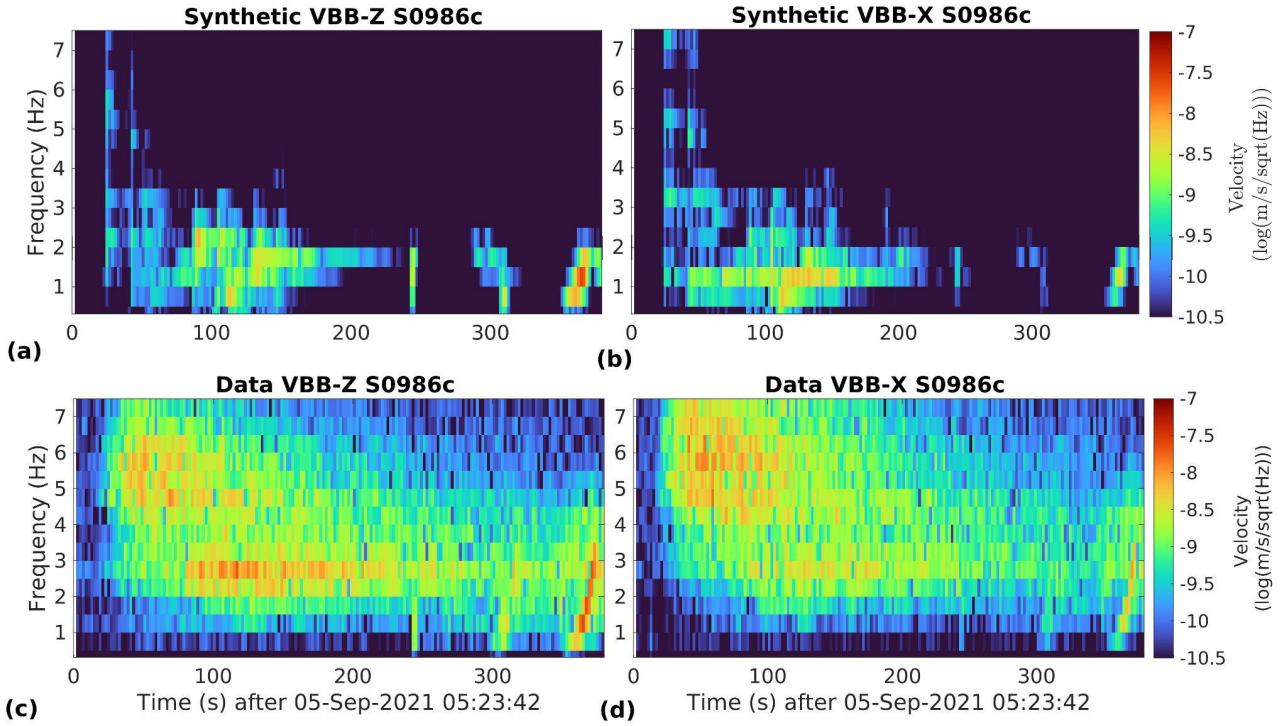

Extended Data Fig. 5| Comparison between simulated and observed vertical and horizontal Vz/Vx spectrograms

Spectrogram of simulated (**a,b**) and observed (**c,d**) vertical (**a,c**) and horizontal (**b,d**) ground velocity along impact direction for event S0986c. Modeling is performed with SPECFEM2D-DG-LNS software.

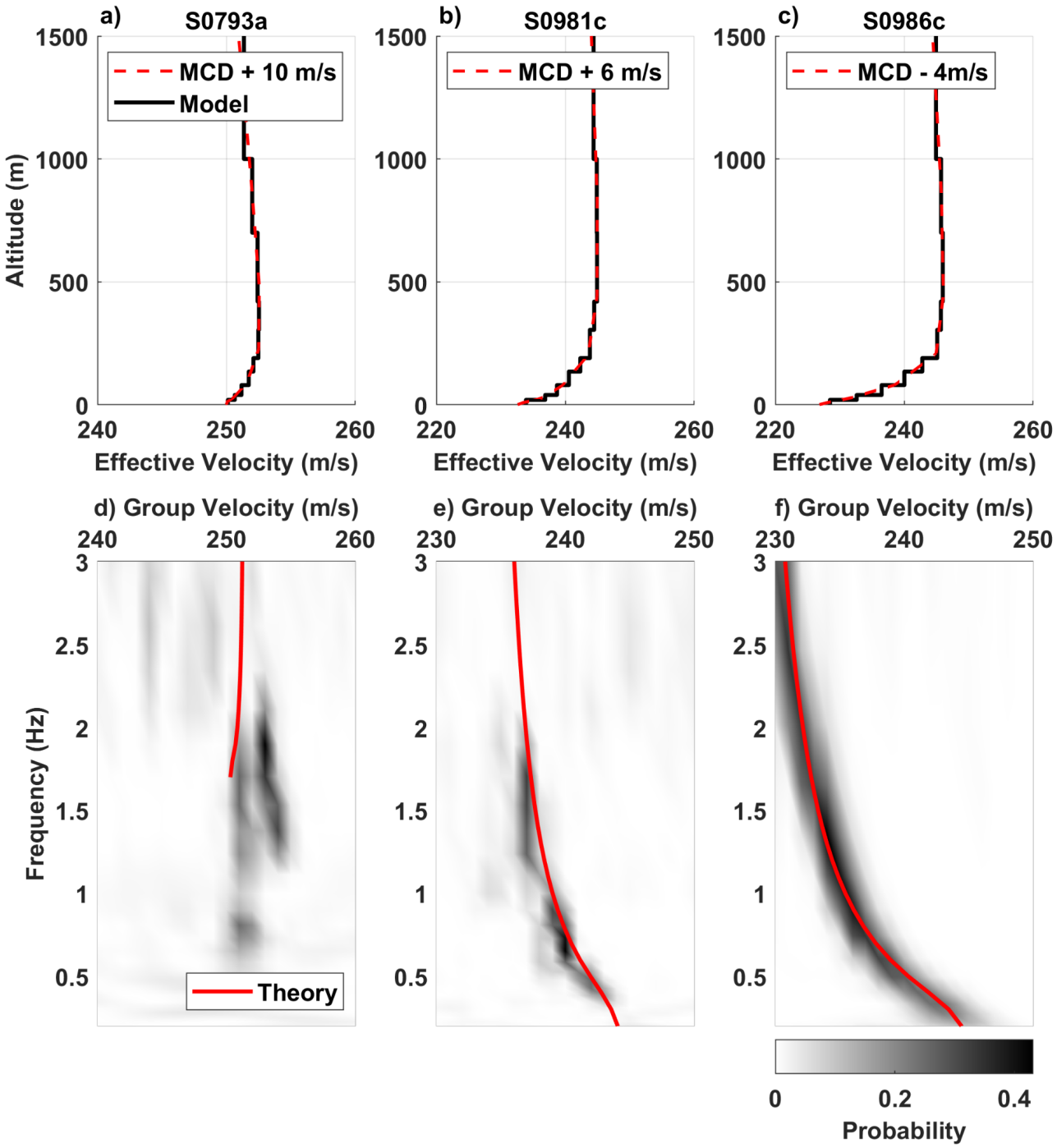

Extended Data Fig. 6| Dispersion of acoustic waves trapped in the surface waveguide

The atmospheric sound speed models and the synthetic and measured group velocities of acoustic guided waves of S0793a, S0981c and S0986c. **a b c** the atmosphere models of effective sound speed (red dashed lines) and the staircase approximation (black lines) for computation of the group velocities. **d e f** the synthetic group velocities (red curve) from the staircase approximation and the group velocity measurements (gray background) from the real data. The gray color intensity indicates the probability of the measurements.

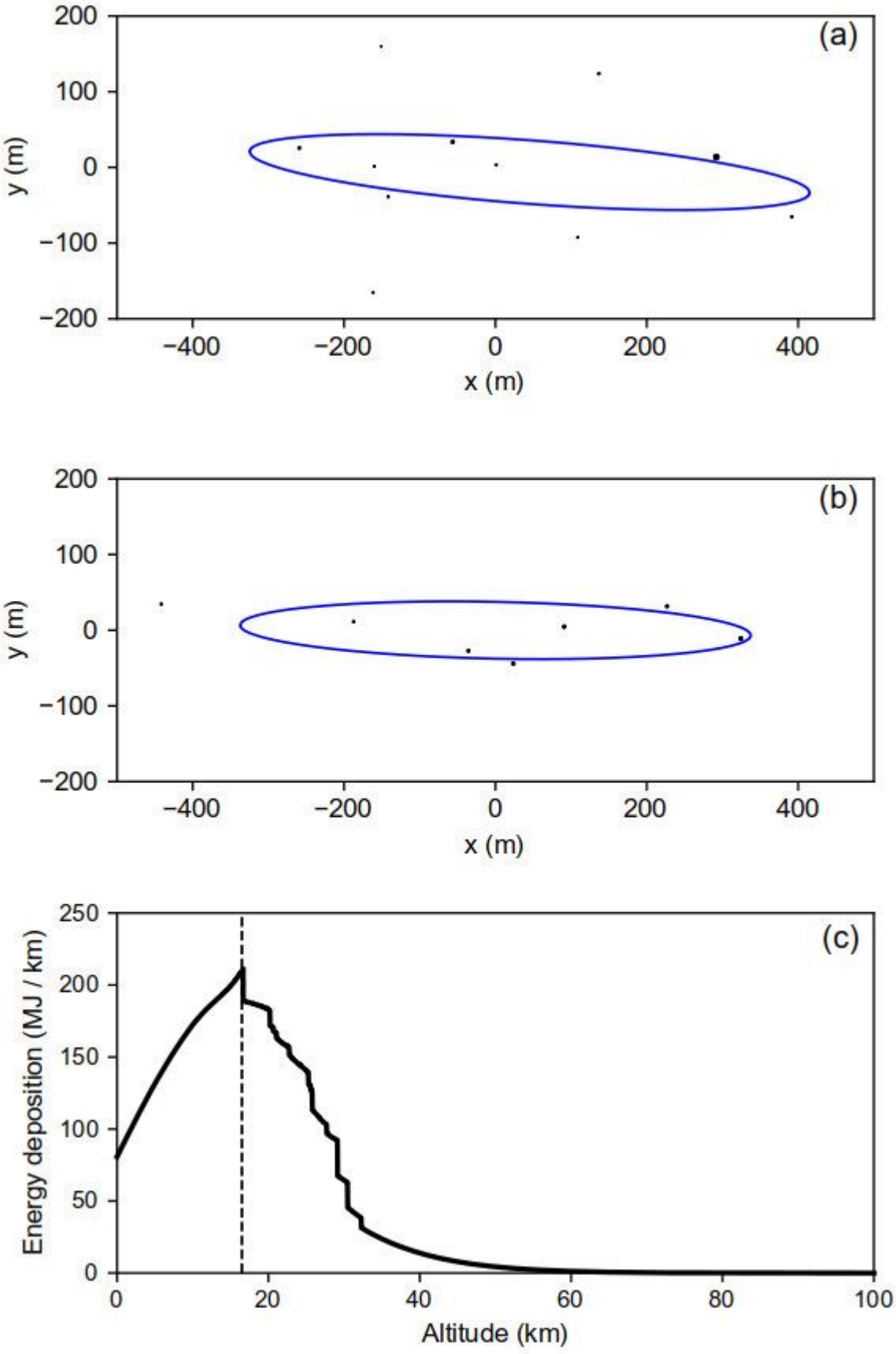

Extended Data Fig. 7 | Meteoroid fragmentation in the atmosphere for S0986c event **a** Size and relative location of craters in the cluster associated with event S0986c, where each circle represents a single crater to scale. **b** An example of a comparable simulated

crater cluster with a similar number of craters >1-m diameter, effective diameter, median separation between craters and aspect ratio of best-fit ellipse (blue). **c** The deposition of meteoroid kinetic energy in the atmosphere associated with the model cluster in **b**, with peak energy deposition at 16.5 km altitude (dashed line).

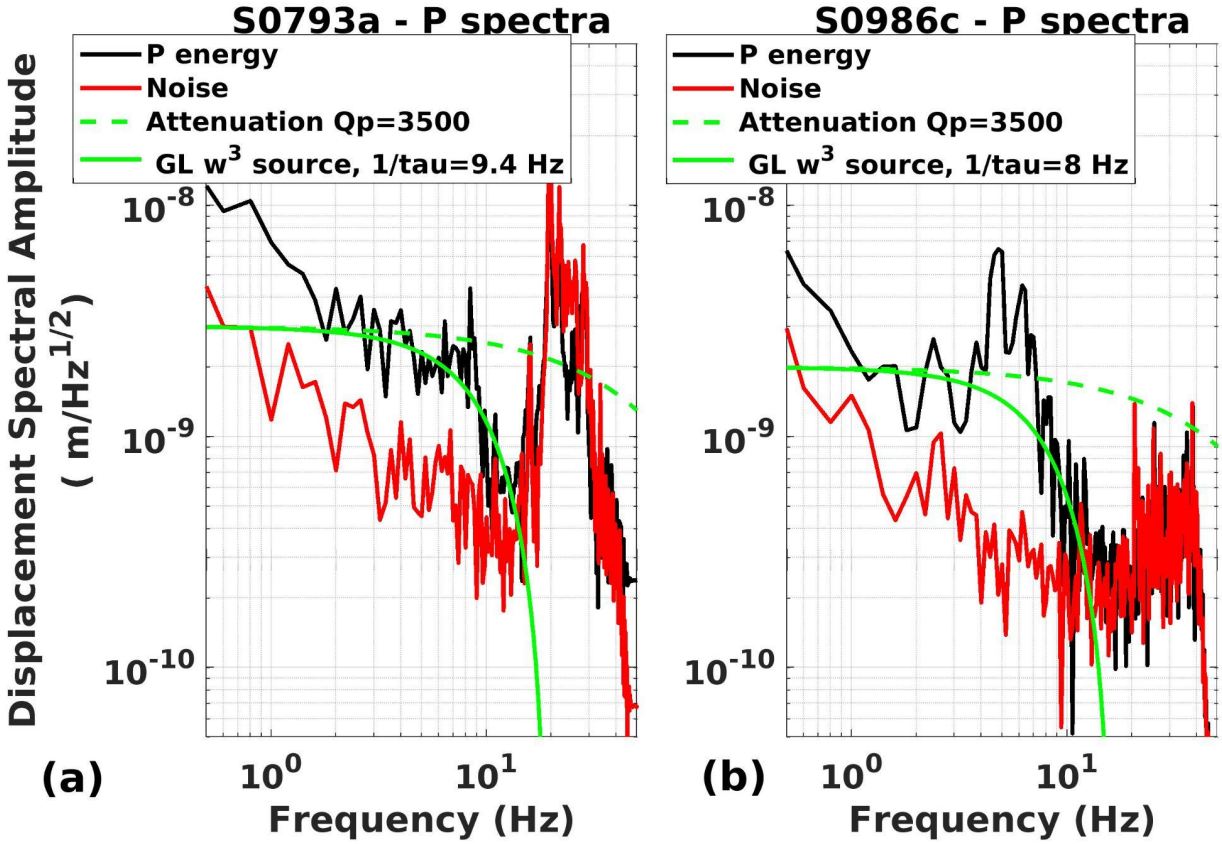

Extended Data Fig. 8 | Estimate of the frequency cutoff of the impact seismic source Displacement spectral amplitudes of P waves of the S0793a event (**a**) and the S0986c event (**b**). Both spectra, in black, are made with a 5 seconds window on deticked 100 sps VBBZ data starting at the MQS P arrival time. The noise spectra in red are estimated by the minimum amplitude of three 5 seconds spectra, computed just before the MQS P arrival time. Note that both the noise before and the signal after the P arrival time of S0793a are corrupted by donks, whose energy appears above 15 Hz, while donks are absent from the records of S0986c around the P arrival time. The green dashed line provides the attenuation cutoff for a Q_p ~ 3300, while the continuous green lines are proposed fit for the f^{-3} source function already proposed for Lunar impacts. An overshoot peaking at 5 Hz and with amplitude increasing with the yield might be compatible with the P wave spectra but need future observations or analysis for confirmation.

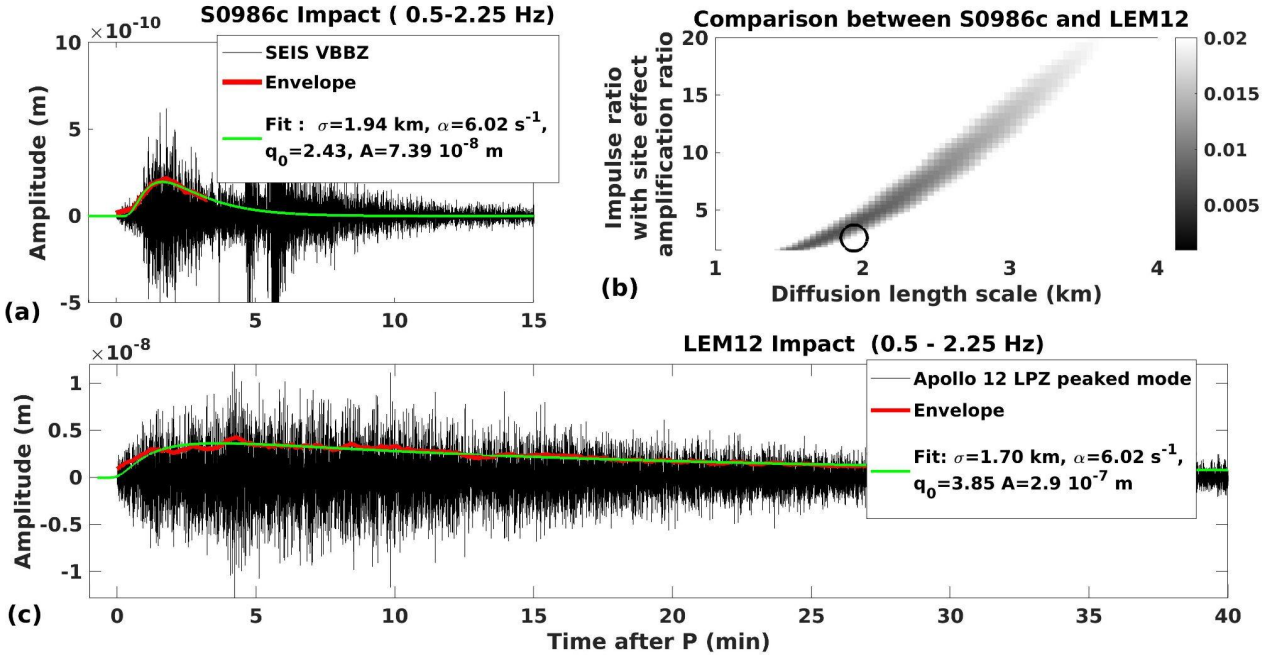

Extended Data Fig. 9. **Comparison between Mars and Lunar seismic signals from impact and constraints on seismic properties and impact seismic source.**
Panel **a** is for the Martian S0986c impact, while panel **b** is for LEM12 impact recorded on the Apollo 12 LP vertical seismometer. Red lines in panels **a** and **b** are the envelope, while the green lines are the modeled envelopes. Panel **c** shows the acceptable solutions, as function of length scale and of the effective source ratio between the two impactors. The Black circle provides the Lunar Diffusion length scale measured for the LEM impact (1.93 km) as well as the 2.57 ratio between the Apollo LEM vertical momentum (230150 Ns) and the estimated one for S0986c (89 500 Ns). Variance reductions better than 98% (in gray in panel **c**) are obtained with a larger attenuation as the one found on the Moon and suggest larger diffusion length scale, depending on the strength of the site effects on the Moon as compared to Mars.

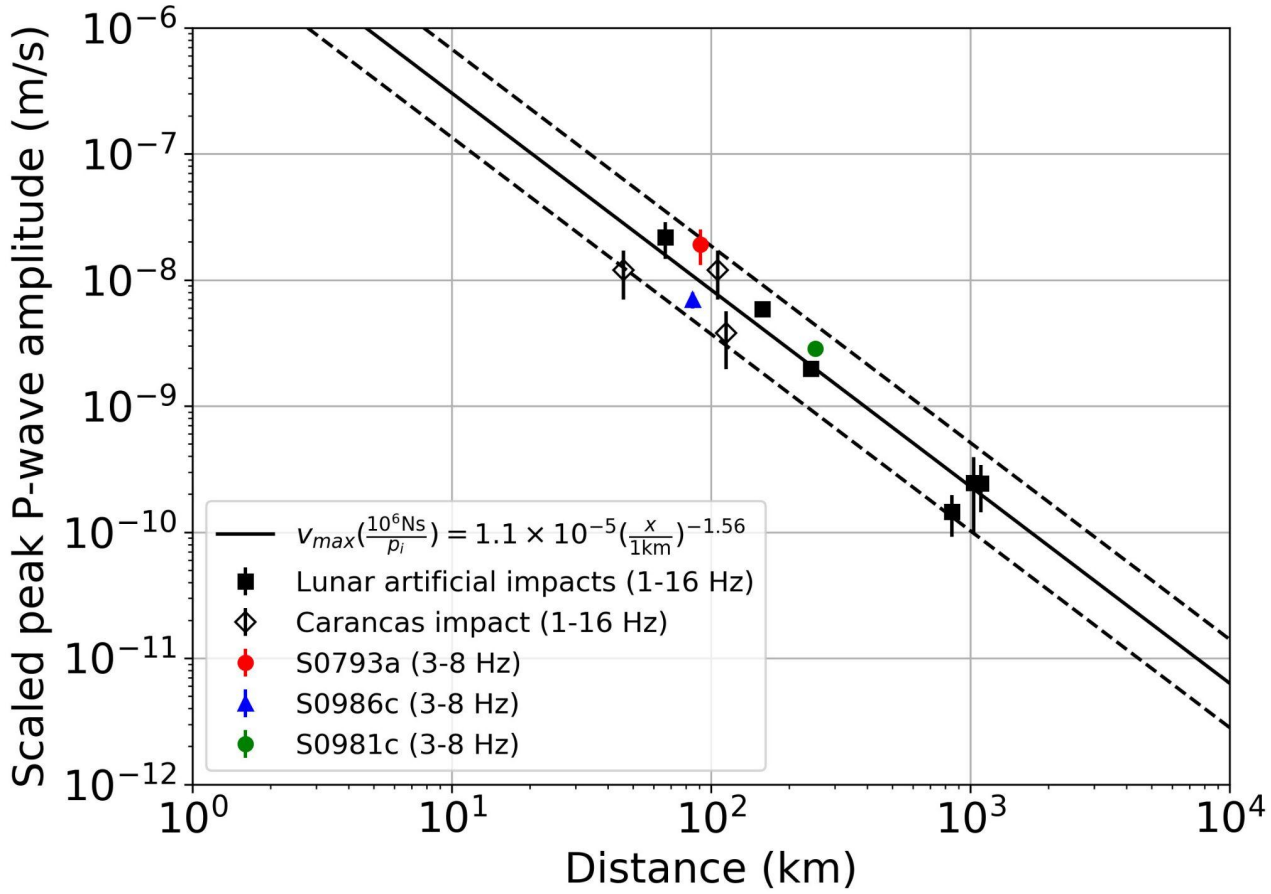

Extended Data Fig. 10 | P-wave amplitude scaling relationship
We propose an updated least squares amplitude-distance scaling relationship [39,40] where peak vertical ground velocity of first arrival P-wave is normalized by total impact momentum (which is scaled by 10^6 Ns), shown as a solid line. The distance from impact is given in km. The dashed lines indicate the factor of two uncertainties. Data points shown include the artificial impacts on the Moon (peak first arrival amplitude between 1-16 Hz; [67]), the Carancas impact (peak first arrival amplitude between 1-16 Hz, [68,69]) and the three events on Mars identified by InSight as impacts (peak first arrival amplitude between 3-8 Hz). The data are provided as measured values +/- uncertainty estimates.

Extended data ZZZ: Movie and sound of Mars vibrations after impact event S0986
Movie of sonified records of ground vertical velocity (time accelerated by a factor 220.5), on top of the image of VBB velocity records, spectrogram of vertical velocity, coherogram of vertical and horizontal components, and phase shift between these two components at maximum coherence. A cursor is moving along the records to indicate where the sound is produced.